Nano Research

ISSN 1998-0124 CN 11-5974/O4
https://doi.org/10.26599/NR.2026.94908831

Racing-car-inspired electrical/chemical dual-driven actuators for swimming Marangoni robots based on carbon nanotube composites

Yuhang Chen[1,2,§], Yongqiang Qian[3,§](✉), Wei Zhang[1,2], Zhiling Luo[1,2](✉), Luzhuo Chen[1,2](✉)

[1] Fujian Provincial Key Laboratory of Quantum Manipulation and New Energy Materials, College of Physics and Energy, Fujian Normal University, Fuzhou 350117, China

[2] Fujian Provincial Engineering Technology Research Center of Solar Energy Conversion and Energy Storage, Fujian Normal University, Fuzhou 350117, China

[3] Fujian Laser Precision Machining Engineering Technology Research Center, College of Intelligent Manufacturing, Putian University, Putian 351100, China

[§] Yuhang Chen and Yongqiang Qian contributed equally to this work.

Nano Res., **Just Accepted Manuscript** • https://doi.org/10.26599/NR.2026.94908831
https://www.sciopen.com/journal/1998-0124 on May. 11, 2026

© The Authors(s)

Just Accepted

Just Accepted

This is a “Just Accepted” manuscript, which has been examined by the peer-review process and has been accepted for publication. A “Just Accepted” manuscript is published online shortly after its acceptance,which is prior to technical editing and formatting and author proofing. Tsinghua University Press (TUP) provides “Just Accepted” as an optional and free service which allows authors to make their results available to the research community as soon as possible after acceptance. After a manuscript has been technically edited and formatted, and the page proofs have been corrected, it will be removed from the “Just Accepted” web site and published officially with volume and article number (e.g., *Nano Research*, **2025**, *18*, 94906990). Please note that technical editing may introduce minor changes to the manuscript text and/or graphics which may affect the content, and all legal disclaimers that apply to the journal pertain. In no event shall TUP be held responsible for errors or consequences arising from the use of any information contained in these “Just Accepted” manuscripts. To cite this anuscript please use its Digital Object Identifier (DOI®),which is identical for all formats of publication.

Racing-car-inspired electrical/chemical dual-driven actuators for swimming Marangoni robots based on carbon nanotube composites

Yuhang Chen[1,2,§], Yongqiang Qian[3,§], Wei Zhang[1,2], Zhiling Luo[1,2], and Luzhuo Chen[1,2]

[1] *Fujian Provincial Key Laboratory of Quantum Manipulation and New Energy Materials, College of Physics and Energy, Fujian Normal University, Fuzhou, 350117, China*
[2] *Fujian Provincial Engineering Technology Research Center of Solar Energy Conversion and Energy Storage, Fujian Normal University, Fuzhou, 350117, China*
[3] *Fujian Laser Precision Machining Engineering Technology Research Center, College of Intelligent Manufacturing, Putian University, Putian, 351100, China*
[§] *Yuhang Chen and Yongqiang Qian contributed equally to this work.*

TABLE OF CONTENTS (TOC)

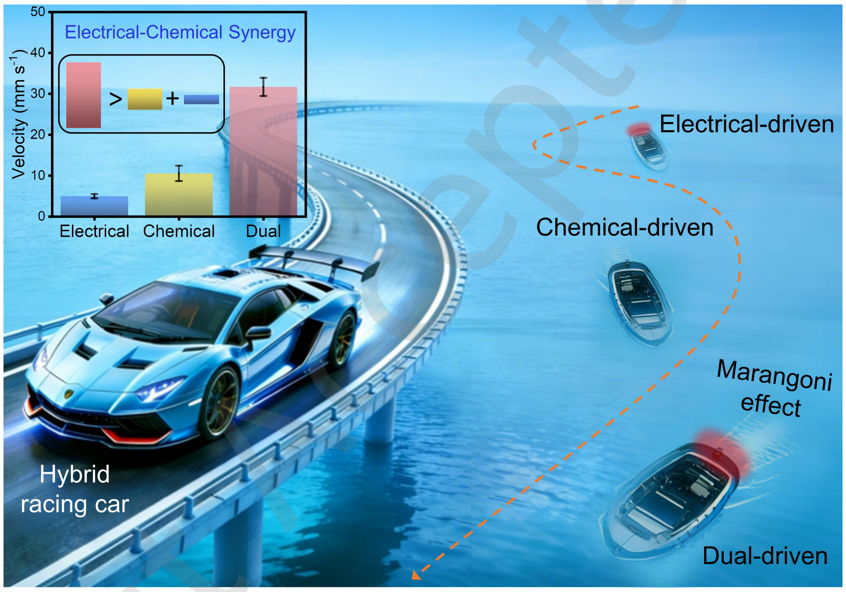

Inspired by the multi-mode propulsion strategies employed in high-performance racing cars, an electrical/chemical dual-driven Marangoni actuator constructed from carbon nanotube-cellulose fiber/polyethylene composite is developed. This actuator exhibits rapid, autonomous swimming locomotion and programmable motion capabilities on water surfaces.

Nano Research

Open Access

Research Article

Racing-car-inspired electrical/chemical dual-driven actuators for swimming Marangoni robots based on carbon nanotube composites

Yuhang Chen[1,2,§], Yongqiang Qian[3,§], Wei Zhang[1,2], Zhiling Luo[1,2], and Luzhuo Chen[1,2]

[1] *Fujian Provincial Key Laboratory of Quantum Manipulation and New Energy Materials, College of Physics and Energy, Fujian Normal University, Fuzhou, 350117, China*
[2] *Fujian Provincial Engineering Technology Research Center of Solar Energy Conversion and Energy Storage, Fujian Normal University, Fuzhou, 350117, China*
[3] *Fujian Laser Precision Machining Engineering Technology Research Center, College of Intelligent Manufacturing, Putian University, Putian, 351100, China*
[§] *Yuhang Chen and Yongqiang Qian contributed equally to this work.*

Received: 12 March 2026; **Revised:** 24 April 2026; **Accepted:** 11 May 2026

Address correspondence to Yongqiang Qian, qianyongqiang@ptu.edu.cn; Zhiling Luo, luozl@fjnu.edu.cn; Luzhuo Chen, ChenLZ@fjnu.edu.cn

Cite this article: *Nano Research*, 2026, 19, 94908831 https://doi.org/10.26599/NR.2026.94908831

ABSTRACT: Swimming robots driven by the Marangoni effect have attracted considerable research interest recently. Current Marangoni actuators are mostly chemical-driven or light-driven. However, simultaneously achieving high actuation speed and programmable motions remains a persistent challenge. Herein, inspired by multi-mode propulsion strategies employed in high-performance racing cars, we propose electrical/chemical dual-driven Marangoni actuators fabricated from carbon nanotube-cellulose fiber (CNT-CF) and polyethylene (PE) composites. Firstly, under electrical stimulation, the actuator exhibits programmable self-propelled swimming locomotion (linear and turning motions) on water surfaces. The actuation mechanism is due to the temperature gradient generated by Joule-heating. Secondly, upon dissolution of an embedded bone glue film, the actuator operates in a purely chemical-driven Marangoni mode, generating rapid autonomous swimming locomotion. Critically, when both electrical and chemical stimuli are applied, the actuator enters a dual-driven mode through a synergistic effect, attaining a velocity of 32.2 mm s^{-1}, exceeding the arithmetic sum of individual electrical-driven (5.4 mm s^{-1}) and chemical-driven (11.3 mm s^{-1}) velocities by over 93%. Furthermore, the same CNT-CF/PE material system can fabricate actuators showcasing on-land crawling motions. Finally, two actuators are assembled to a functional robotic gripper, demonstrating the versatility of platform. This work establishes a unified design paradigm for state-of-the-art actuators and multifunctional amphibious devices.

KEYWORDS: actuator, carbon nanotube, dual-driven, Marangoni effect, swimming robot

1 Introduction

As one of the core components of robots, actuators are evolving toward intelligence, miniaturization, and multifunctionality, which are propelled by rapid advancements in intelligent technologies [1-4]. They can respond to external stimuli (such as light [5, 6], electricity [7], magnetic fields [8], and humidity [9]) to achieve various forms of motion, including bending, moving, rotation, and more. Among various actuating systems, polymer-based bilayer or multilayer actuators are widely used in fields such as flexible electronics, soft robotics, and adaptive systems [10-12]. Compared to traditional materials such as shape memory alloys [13] and homogeneous elastomers [14, 15], these actuators feature exceptional design flexibility, diverse motion modes, mild operating conditions, and remarkable cost advantages. Based on different actuation strategies, two categories of actuators have gradually attracted the attention of researchers in recent years. One type is the thermomechanical actuator, which generates periodic bending deformation through volumetric mismatch caused by differences in the coefficient of thermal expansion (CTE) between dissimilar materials [16, 17]. The other category comprises Marangoni actuators, which rely on the Marangoni effect induced by liquid surface tension gradients for actuation [18]. The latter are especially suitable for liquid environments, as they function without any transmission components and exhibit highly flexible, deformation-independent characteristics. In particular, they showcase remarkable performance in water surface motion, having become a hot topic in cutting-edge fields such as aquatic robotics, targeted drug delivery, and microfluidics.

At present, the typical actuation modes of Marangoni actuators remain primarily light-driven [19, 20] and chemical-driven [21] modes, which are relatively limited in form. In particular, light-driven Marangoni actuators employ photothermal materials to transform light energy into localized heat, forming a temperature gradient field at the water-air interface. Leveraging the property that surface tension decreases with increasing temperature, a surface tension gradient spontaneously generates between the hot and cold areas, propelling the actuator toward a specific direction. For example, Li et al. proposed an asymmetric light-driven ship fabricated by a polymer cross-linked with Fe^{3+}/catechol coordination bonds, which enables multiple motion modes including forward, backward, rotation, and crossing the water/air interface [22]. This device was integrated into smart transportation and contactless delivery. In contrast, chemical-driven Marangoni actuators draw inspiration from the propulsion mechanism of the rove beetle. These insects enable rapid motion across water surfaces by precisely regulating the secretion of quinone compounds, which serve as chemical “fuel”, from abdominal glands to instantaneously reduce local surface tension. For instance, Floreano et al. reported a biodegradable, edible aquatic robot powered by freeze-dried fish food as “fuel”, autonomously releasing surfactants to propel rapid motion across water surfaces [23]. Nevertheless, these Marangoni actuators face inherent limitations. Firstly, light-driven Marangoni actuators typically require continuous, precise localized irradiation, with limited energy input density and susceptibility to spot drift interference. Secondly, the chemical-driven Marangoni actuators are constrained by the uncontrollable diffusion process of the “fuel” and the rapid decay of propulsion force. These limitations make it challenging for single-mode Marangoni actuators to balance both motion speed and controllability. A simultaneous optimization of autonomous programmability and rapid responsiveness within a single Marangoni actuator remains a rare achievement.

Combining stimulus-responsive materials with the chemical Marangoni effect presents an ideal strategy for addressing the above challenges. Stimulus-responsive materials can function as intelligent “switches”, precisely regulating the release speed and location of chemical “fuel” under external field signals such as light, heat, and electricity, thereby achieving efficient and economical actuation. Furthermore, stimulus sources (such as laser spots, circuit arrays, and magnetic fields) can be precisely programmed in

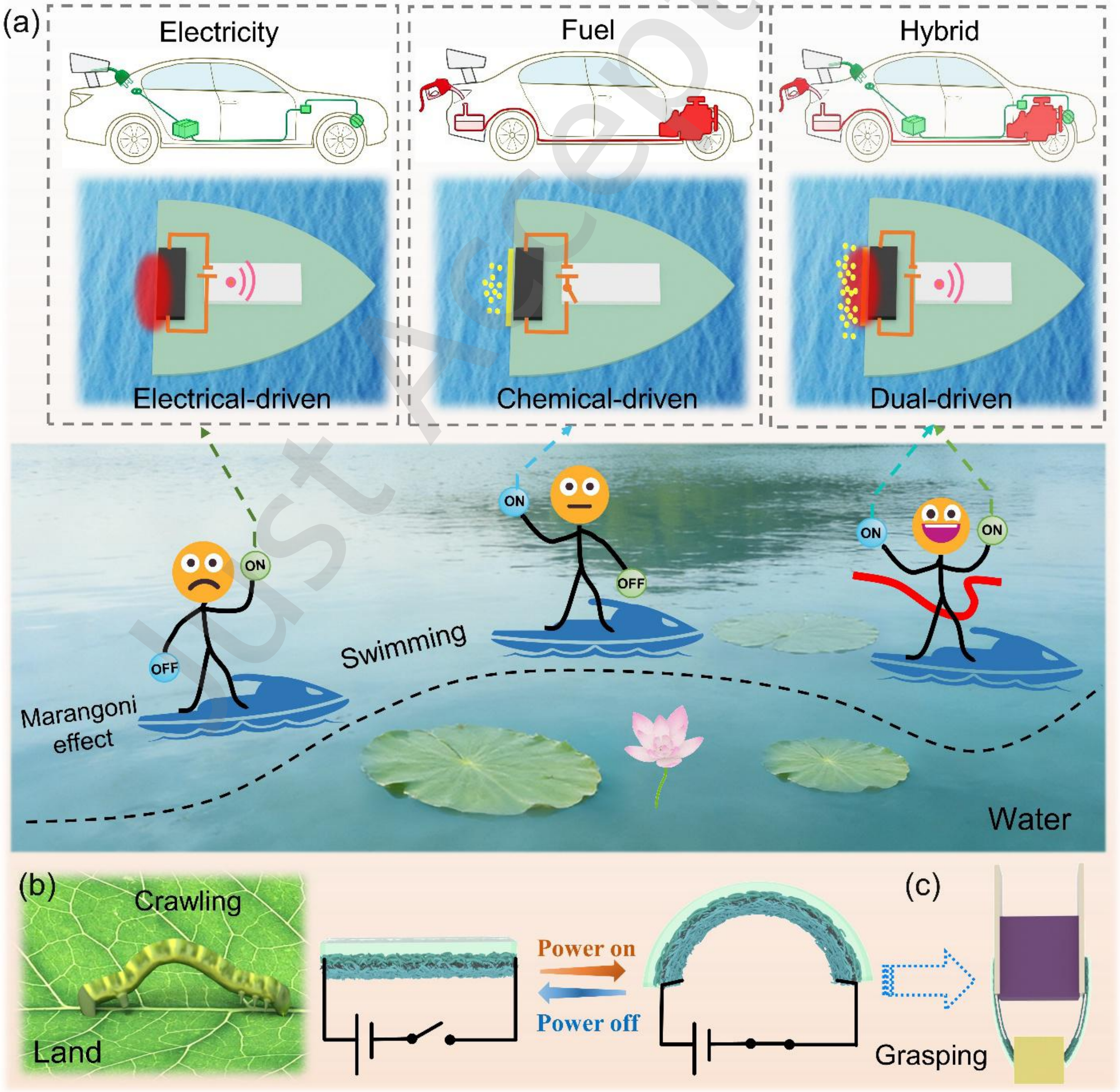

Scheme 1 (a) Schematic of an electrical/chemical dual-driven Marangoni CNT-CF/PE actuator inspired by multi-mode propulsion strategies in racing cars. (b) The CNT-CF/PE actuator mimicking inchworm crawling on land and (c) A robotic gripper based on CNT-CF/PE actuators.

both time and space, markedly improving the remote-control accuracy of the macroscopic motion trajectory for actuators. More importantly, stimulus-responsive materials can simultaneously integrate multimodal functions including self-healing and environmental sensing, endowing the actuator with higher levels of autonomy and adaptability to the environment. Based on the above strategy, Zhang et al. constructed a cavity structure using graphene/polydimethylsiloxane photothermal composites, employing filament light sources as triggers to control the pulsed release of ethanol “fuel”. A light-driven and programmable insect-scale Marangoni swimming robot was successfully developed [24]. Zhong et al. designed a leaf-like shape small-scale on-water robot powered by a programmable Marangoni motor. Controlling the temporal release of ethanol “fuel” through pulsed channels via electromagnetic effects enabled controllable propulsion, smart sensing, and even wireless communication functions [25]. However, the volatility of liquids such as ethanol limits “fuel” lifetime, while leakage risks pose environmental and biosafety issues. Meanwhile, liquid storage and microchannel sealing structures greatly increase manufacturing complexity and system integration challenges. In contrast, solid “fuels” (e.g., bone glue and other biomass materials) are attracting increasing research interest due to their excellent biocompatibility, degradability, and potential for high integration with small-scale robotic architectures [26, 27]. Unfortunately, the slow dissolution rate of solid “fuels” results in insufficient release intensity, and the limited amplitude of surface tension perturbations struggles to meet the demands of high-speed, heavy-load actuation. These factors remain major constraints on their practical application.

Herein, inspired by the racing cars which have multi-mode propulsion strategies (i.e., electric, fuel, and hybrid), we report a composite material composed of carbon nanotube-cellulose fiber (CNT-CF) and polyethylene (PE) film, which functions as a dual-driven Marangoni actuator and can be further used for amphibious applications. This Marangoni actuator possesses independent electrical-driven and chemical-driven modes. More importantly, it can convert electrical stimuli into Joule-heating within the CNT-CF film, generating localized temperature gradients to propel surface motion while precisely regulating the release of chemical “fuel” on the water surface. Thus, synergistic enhancement effects are achieved through electrical/chemical dual-driven systems (Scheme 1a). Furthermore, through asymmetric structural design, this Marangoni actuator can execute programmable self-propelled swimming locomotion, such as linear motion and turning motions. Notably, we further developed a CNT-CF/PE actuator that mimics the on-land directional crawling of inchworms (Scheme 1b). Moreover, two CNT-CF/PE-based actuators together can be assembled into a robotic gripper (Scheme 1c), embodying the design idea of one material serving multiple purposes.

2 Experimental Section

2.1 Materials and reagents

Multi-walled carbon nanotubes were purchased from Chengdu Organic Chemicals Co. Ltd., Chinese Academy of Sciences. The bone glue was purchased from Zhejiang Hongyun Chemical Co., Ltd. The ethanol (75%) was purchased from Changshu Xinyuhua Import and Export Co. Ltd. The cellulose paper was purchased from Shenzhen Liwu Industrial Co., Ltd. The PE film with adhesive was purchased from Shenzhen Zhenhua Adhesive Products Co. Ltd. The wireless remote-control device was purchased from Shenzhen Chuangliwei Wireless Electronic Technology Co. Ltd. The miniature lithium battery was purchased from Shenzhen Xinlechuang Technology Co. Ltd. All water used was deionized water.

2.2 Preparation of the CNT-CF composite film

First, the CF (shredded cellulose paper, 150 mg) and CNT (600 mg) were added to ethanol (75%, 200 mL) and mixed together. Then, this mixture was dispersed by ultrasonication for 10 min. Second, the excess ethanol solution was removed by vacuum filtration. Finally, the CNT-CF (4:1) composite film was obtained by drying for 30 min at 40 °C. Notably, CNT-CF composite films with other ratios were prepared using the same method. The specific masses of the CNTs and CF used are as follows. For the CNT-CF (1:1), CNT (375 mg) and CF (375 mg) were used. For the CNT-CF (2:1), CNT (500 mg) and CF (250 mg) were used. For the CNT-CF (3:1), CNT (562.5 mg) and CF (187.5 mg) were used. For the CNT-CF (5:1), CNT (625 mg) and CF (125 mg) were used.

2.3 Preparation of the bone glue film

First, the bone glue granules (1 g) were added to deionized water (9 g) and completely dissolved in hot water (80 °C) to obtain the bone glue solution (10 wt%). Second, the solution was transferred to a clean Petri dish (10 cm × 10 cm) and cooled to room temperature for 24 h. Finally, a solid-state bone glue film with a thickness of ~32 μm was obtained.

2.4 Measurement of the dissolution rate of bone glue film under different water temperatures

First, five beakers containing deionized water (500 mL) were placed in a water bath and heated to 25 °C, 35 °C, 45 °C, 55 °C, and 65°C, respectively. Second, five pieces of bone glue film were placed into the corresponding beakers. The dimension of each bone glue film was 2 cm × 1 cm × 32 μm, with a mass of ~19 mg. Finally, the complete dissolution time of each sample was recorded.

2.5 Preparation of the linear motion Marangoni actuator

First, the PE film was cut into the bullet shape shown in Fig. S1(a) in the Electronic Supplementary Material (ESM). Then, the CNT-CF composite film (2 cm × 0.5 cm) was fixed to the center of the tail part of PE film. The two ends of the CNT-CF film were connected to a wireless module and a micro-power source (chargeable miniature lithium battery) using conductive silver adhesive. Notably, the chemical-driven Marangoni actuators were prepared by fixing additional bone glue films (2 cm × 0.5 cm, 2 cm × 0.75 cm, and 2 cm × 1 cm) to the tails of the above-described actuators, as illustrated in Fig. S1(b-d) in the ESM. The dual-driven Marangoni actuator was prepared by fixing an additional bone glue film (2 cm × 1 cm). In these cases, the length of the exposed portion of the bone glue film was approximately 0.5 cm.

2.6 Preparation of the turning motion Marangoni actuators

The dimensions of the PE film were the same as that described in the above section. Three CNT-CF composite films with dimensions of 1 cm × 0.5 cm were fixed onto the tail of the PE film at equal intervals with an adjacent spacing of ~0.5 cm. The closed circuits formed by the three CNT-CF films and the micro-power source were each controlled via a wireless module.

2.7 Preparation of the crawling actuator

First, a CNT-CF composite film was attached to a PE film (4 cm × 1 cm). Then, copper electrodes were fixed to both ends of the CNT-CF/PE composite film with conductive silver adhesive, and it was connected to a small direct-current regulated power supply.

2.8 Preparation of the robotic gripper

First, two strips of CNT-CF composite film were cut and combined with PE films (3 cm × 1 cm). Then, they were shaped into U-shaped structures. Copper electrodes were attached to both ends of each structure using silver adhesive, and the structures were fixed to opposite sides of an insulating foam block to serve as the gripper.

2.9 Measurement of on-water motion based on Marangoni effect

All on-water experiments were conducted in an acrylic tank with dimensions of 40 cm × 40 cm × 5 cm (length × width × height) and filled with deionized water. An iPhone 16 Pro was used to record the motion process. Motion data were analyzed using video analysis software. The ambient temperature for the experiments was ~ 21 °C.

3 Results and Discussion

The CNTs used are multi-walled CNTs, which are one-dimensional nanostructures composed of concentric tubular structures formed by the curling of multi-layered graphene [28]. This material exhibits outstanding mechanical and thermal properties, making it an ideal photothermal material. However, owing to their extremely high surface energy and strong intertube van der Waals forces, conventional CNT networks tend to structural collapse induced by capillary forces during drying [29]. Additionally, CNTs exhibit strong interfacial adhesion with most substrates. Currently, large-area, intact, self-supporting pure CNT films are challenging to obtain. The CF, a widely available, biodegradable

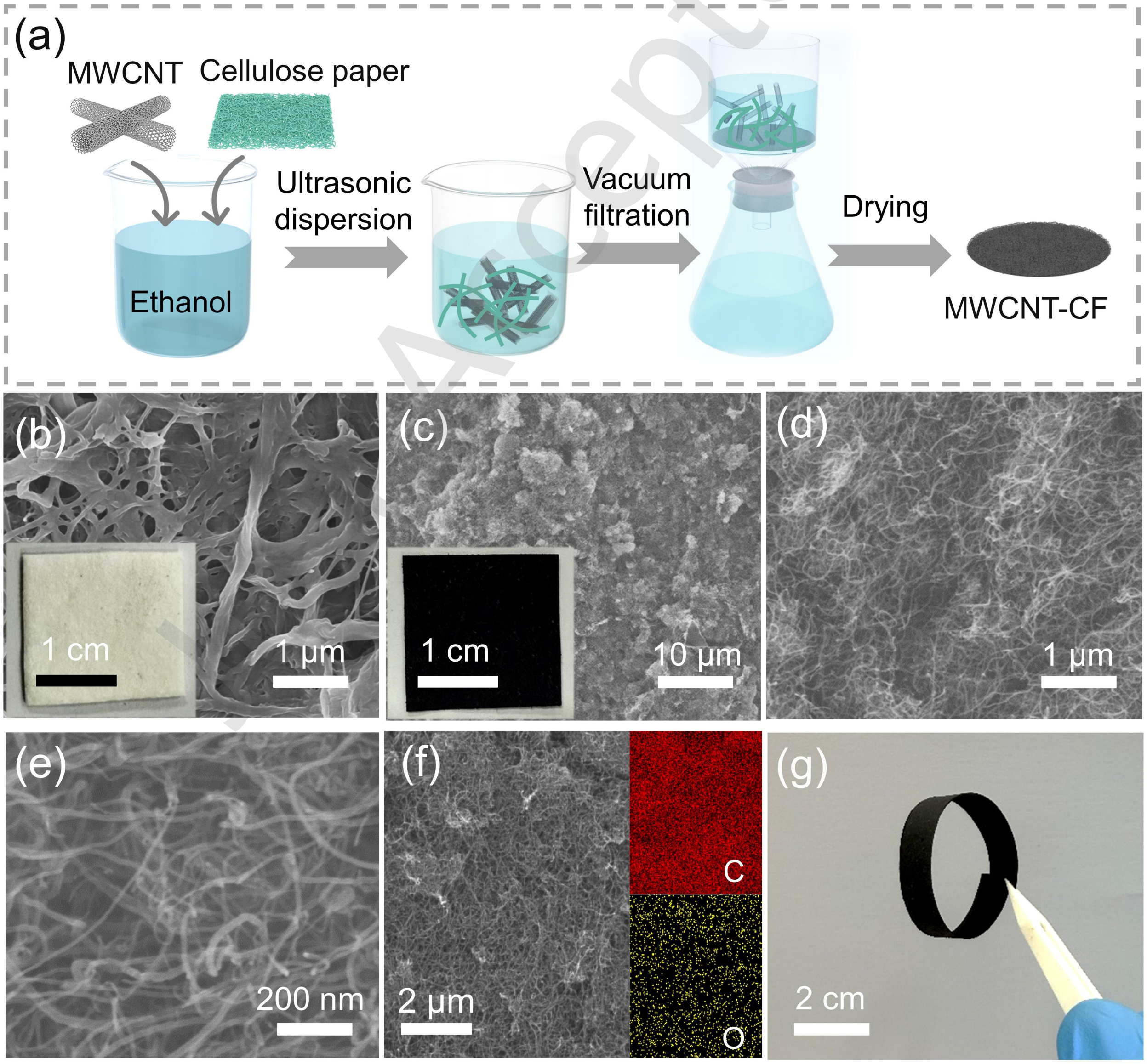

Figure 1 (a) Schematic of the preparation process for CNT-CF composite film. (b) Surface SEM image and optical photograph of pristine CF film. (c) Low-magnification SEM image and optical photograph of CNT-CF composite film. (d) Medium-magnification SEM image of the CNT-CF composite film. (e) High-magnification SEM image of the CNT-CF composite film. (f) SEM image of the CNT-CF composite film and corresponding elemental mapping of

C and O. (g) Optical photograph of the CNT-CF composite film in a bent state, demonstrating its excellent flexibility.

green material, offers abundant active sites [30]. The three-dimensional (3D) crosslinked network constructed from CF provides excellent substrate support. Fig. 1(a) illustrates the preparation process of the CNT-CF composite film. Specifically, CNTs and CF were firstly added together to ethanol solution and uniformly dispersed by ultrasonic treatment. Secondly, excess ethanol solution was removed from the CNT-CF mixture via vacuum filtration. Finally, the self-supporting CNT-CF composite film was obtained after drying. The experiment details are provided in the Experimental Section. Notably, the mass ratio of CNT and CF used in this study is 4:1. Detailed explanations will be provided in the following sections. As shown in Fig. 1(b), the scanning electron microscopy (SEM) image clearly reveals the pore structure of the pristine CF film obtained by vacuum filtration of CFs without CNTs. The inset of Fig. 1(b) is an optical photograph of the pristine CF film. The surface SEM image of the CNT-CF composite film reveals CNTs tightly bound to CFs (Fig. 1(c)). Medium-magnification SEM image shows no obvious agglomeration, indicating uniform dispersion of CNTs within CF (Fig. 1(d)). Additionally, high-magnification SEM clearly displays tubular CNTs interwoven with CF to form a 3D porous network (Fig. 1(e)), providing structural support for the excellent mechanical properties of the composite film. The SEM images showing the microstructures of CNT-CF composite films with other (CNT:CF) ratios are illustrated in Fig. S2 in the ESM. The results indicate that at a larger CF content (CNT:CF = 1:1), poorer dispersion occurs, with noticeable CF agglomeration observed. As the CF content decreases, the uniformity of CNT and CF dispersion significantly improves. However, when the CF content is too low (CNT:CF = 5:1), microcracks begin to appear in the composite film, reducing film continuity.

Energy-dispersive X-ray spectra (EDS) was used for micro-area elemental analysis of the CNT-CF composite film (Fig. 1(f)). The uniform distribution of C and O elements, with oxygen primarily distributed on the CF surface, further confirms the homogeneous composite of CNT and CF. Moreover, benefiting from the synergistic reinforcement and toughening effects between CF and CNT, the CNT-CF composite film exhibits excellent mechanical flexibility, capable of freely bending as shown in Fig. 1(g). These properties are primarily attributed to the 3D interlocking structure formed by one-dimensional CNT interweaving and entangling with CF. In addition, the CF can be firmly bonded to CNT through interfacial interactions via its surface-rich functional groups, such as hydroxyl groups [31, 32].

X-ray diffraction (XRD) patterns and Raman spectra confirmed the successful composite formation of CNT with CF. As shown in Fig. 2(a), the pristine CF exhibits the classical crystalline structure of cellulose I [33, 34]. The characteristic peaks at 15.6°, 22.5°, and 34.1° correspond to the (110), (200), and (004) crystal planes, respectively. Furthermore, the CNT-CF composite film exhibits characteristic peaks of cellulose I, as well as typical graphite-like crystalline peaks at 26.0° and 42.9°, attributable to (002) and (100) crystal planes, respectively. These results indicate that the crystal structure of CF remains unchanged after CNT composite formation. The Raman spectra of pristine CF and CNT-CF composite films are presented in Fig. 2(b). As a polysaccharide, cellulose exhibits characteristic Raman bands at 1000-1200 cm^{-1} corresponding to the asymmetric stretching of υ(C-O-C) and the υ(C-C) stretching. The 1300-1500 cm^{-1} range corresponds to the δ(CH_2) and δ(CH_2OH) deformations. This is consistent with previously reported results [34, 35]. Additionally, the CNT-CF composite film exhibits sharp characteristic peaks at 1350 cm^{-1} and 1580 cm^{-1}. These are attributed to the D band and G band of CNT, respectively, indicating graphite lattice defects and interlayer coupling effects [36].

To further optimize the performance of the composite material, the electrical and mechanical properties of CNT-CF composite films with different ratios were investigated. As shown in Fig. 2(c), the results indicate that the electrical properties of the composite films gradually improve as the

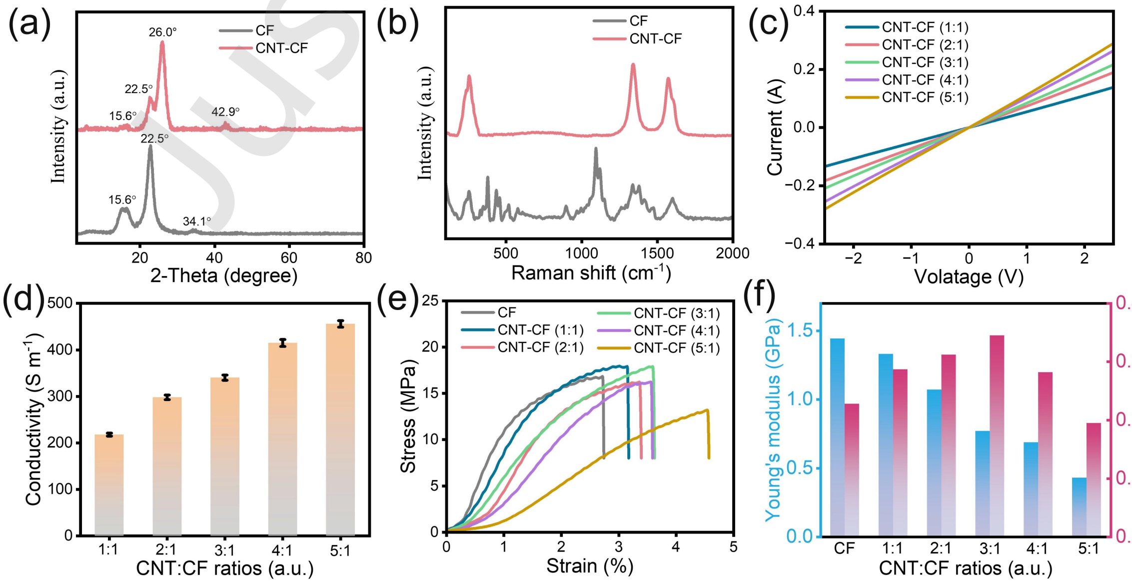

Figure 2 (a) XRD patterns of pristine CF film and CNT-CF composite film. (b) Raman spectra of pristine CF and CNT-CF composite film. (c) Output current as a function of voltage for CNT-CF (1:1), CNT-CF (2:1), CNT-CF (3:1), CNT-CF (4:1), and CNT-CF (5:1) composite films. (d) Conductivities of CNT-CF (1:1), CNT-CF (2:1), CNT-CF (3:1), CNT-CF (4:1), and CNT-CF (5:1) composite films. (e) Tensile stress-strain curves for pristine CF film, CNT-CF

(1:1), CNT-CF (2:1), CNT-CF (3:1), CNT-CF (4:1), and CNT-CF (5:1) composite films. (f) Young's modulus and toughness of pristine CF film, CNT-CF (1:1), CNT-CF (2:1), CNT-CF (3:1), CNT-CF (4:1), and CNT-CF (5:1) composite films.

CNT content increases. Specifically, the conductivities of CNT-CF (1:1), CNT-CF (2:1), CNT-CF (3:1), CNT-CF (4:1), and CNT-CF (5:1) were measured as 217.8 S m^{-1}, 297.9 S m^{-1}, 340.3 S m^{-1}, 414.8 S m^{-1}, and 455.7 S m^{-1}, respectively (Fig. 2(d)). The calculation process is provided in Note S1 in the ESM. Additionally, the surface temperatures of these five composites were recorded after applying a voltage of 3.7 V for 5 s (Fig. S3 in the ESM). The results demonstrate that higher conductivity promotes greater Joule-heating generation under constant voltage conditions.

Furthermore, the tensile stress-strain curves were analyzed to quantitatively characterize the mechanical properties of the materials, as shown in Fig. 2(e). Obviously, as the CNT content increases, the Young's modulus of the composites gradually decreases, while their toughness exhibits a trend of first increasing and then decreasing (Fig. 2(f)). Specifically, the Young's modulus of pristine CF film is 1.44 GPa, with a toughness of 0.23 MJ m^{-3}. The Young's modulus of CNT-CF (1:1) is 1.32 GPa, with toughness of 0.29 MJ m^{-3}. The Young's modulus of CNT-CF (3:1) is 0.77 GPa, with toughness of 0.35 MJ m^{-3}. Meanwhile, the Young's modulus of CNT-CF (4:1) is 0.69 GPa, with toughness of 0.28 MJ m^{-3}. This phenomenon is attributed to the synergistic effect of reinforcement and toughening between CNT and CF [31, 37]. Specifically, the introduction of CNT typically reduces the compactness of the CF film, leading to a gradual decrease in the Young's modulus of the composite film. However, small amounts of CNT enhance the toughness of the CF film. The uniform dispersion and incorporation of CNT effectively harness their high strength and bridging capability to

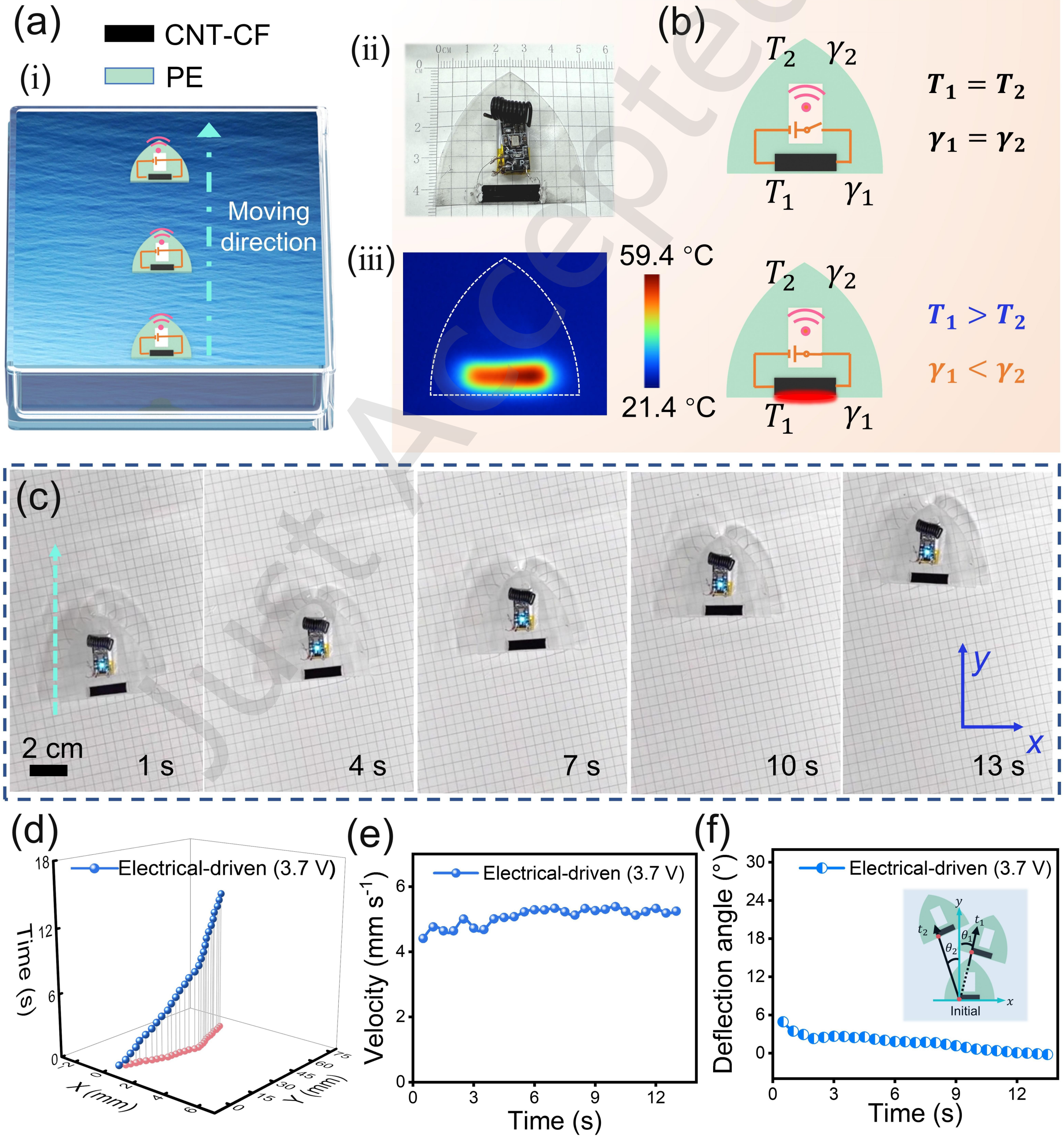

Figure 3 (a) Schematic of the on-water motion for the electrical-driven Marangoni actuator. (b) Schematic illustrating the actuation mechanism of the

electrical-driven Marangoni actuator. (c) Optical photograph of the electrical-driven Marangoni actuator moving across the water surface. (d) Trajectory of the electrical-driven Marangoni actuator. (e) Velocity of the electrical-driven Marangoni actuator as a function of time. (f) Real-time deflection angle of the electrical-driven Marangoni actuator as a function of time, inset showing deflection angle measurement.

dissipate energy. When the CNT content is excessive, the continuous toughening matrix of the CF network becomes disrupted. The CNT network is sparsely bonded by CF, ultimately reducing toughness and film formation. Despite the highest toughness observed in CNT-CF (3:1) composite films, CNT-CF (4:1) composite films were selected as the target material in this study to balance electrical properties. More importantly, the radar charts for CNT-CF films with different ratios also clearly demonstrate that the CNT-CF (4:1) composite film possesses the optimal overall performance (Fig. S4 in the ESM). Based on these results, the CNT-CF (4:1) composite films were used for subsequent development of actuators.

Owing to the surface tension gradient at the interface, the Marangoni effect can propel objects on water surfaces to spontaneously move from areas of low surface tension toward those of high surface tension, demonstrating great potential in fields such as micrometer/nanometer-scale actuation and aquatic robotics. However, poor controllability and slow motion speeds limit practical applications. To address these issues, minimizing motion resistance and enhancing the precision of heating locations are required. Compared to light and magnetic fields, electricity offers high controllability. Furthermore, by controlling the heating location and energization duration, the direction and activation/deactivation of the actuator can be freely regulated.

Inspired by streamlined structures, we developed a bullet-shaped electrical-driven Marangoni actuator based on CNT-CF composite and PE films to achieve directional motion on water surfaces. A schematic is shown in Fig. 3(a-i). Fig. 3(a-ii) illustrates an optical photograph of the electrical-driven actuator. An infrared image clearly reveals the temperature distribution during the actuator operation (Fig. 3(a-iii)). Notably, power-on and power-off of the actuator are remotely controlled via a single-channel wireless module, in which the components are depicted in Fig. S5 in the ESM. In particular, the micro-power supply operates at a voltage of 3.7 V and is reusable (Fig. S6 in the ESM). Fig. S1(a-b) in the ESM shows the dimensional design parameters for the bullet-shaped PE film and the linear-motion Marangoni actuator.

The actuation principle of the electrical-driven Marangoni actuator is illustrated in Fig. 3(b). Initially, the surface tensions at the tail (γ_1) and head (γ_2) of the Marangoni actuator are equal, as the tail temperature (T_1) and head temperature (T_2) remain unchanged. When an electrical stimulus is applied to the CNT-CF film at the tail of the actuator,

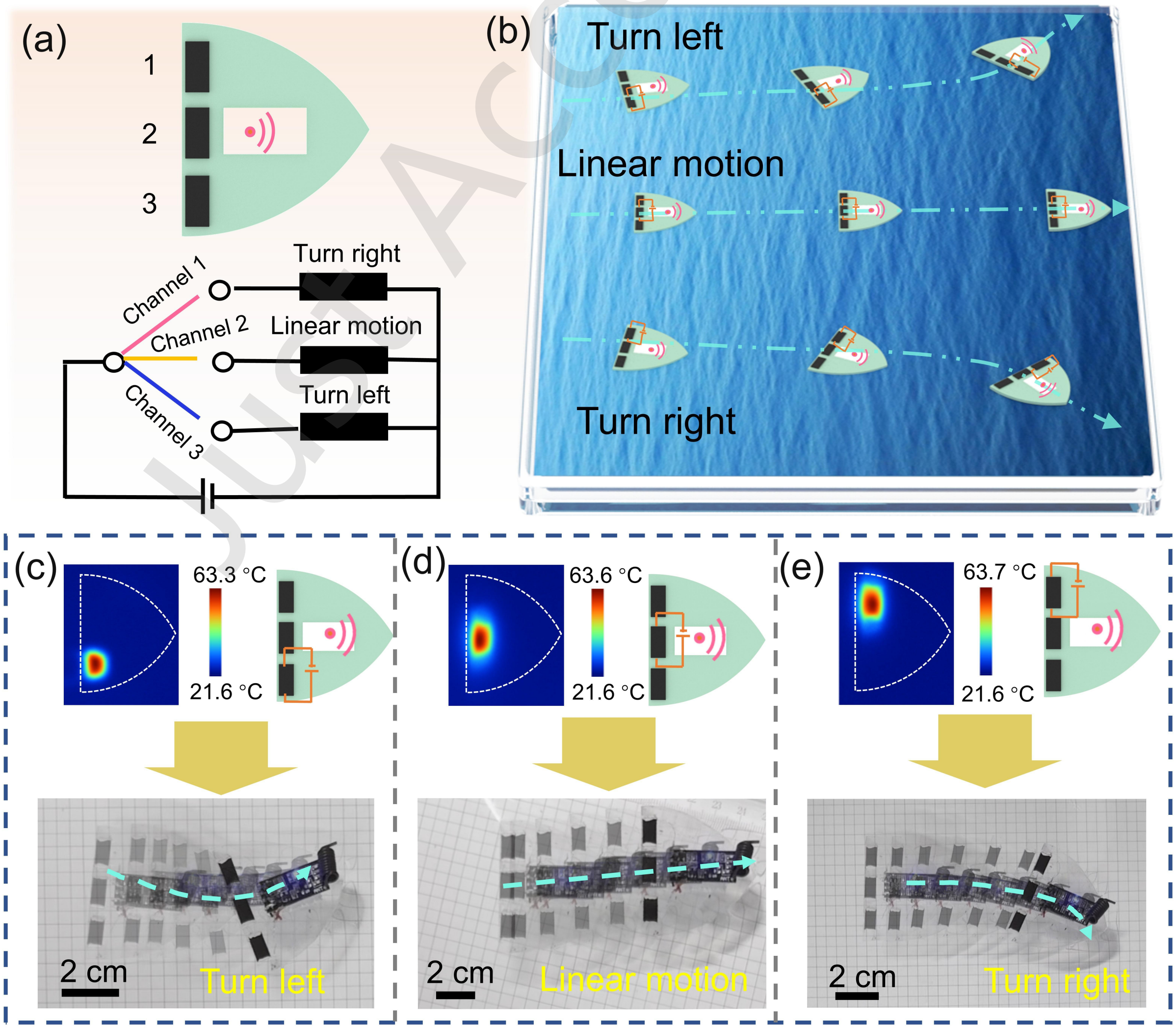

Figure 4 (a) Schematic diagram illustrating the actuation mechanism of the electrical-driven Marangoni actuator with different motion modes. (b) Schematic diagrams of the turning-left, linear and turning-right processes for the electrical-driven Marangoni actuator. (c) Optical photographs, infrared image and corresponding circuit diagram of the actuator during turning-left motion on the water surface. (d) Optical photographs, infrared image and corresponding circuit diagram of the actuator during linear motion on the water surface. (e) Optical photographs, infrared image and corresponding circuit diagram of the actuator during turning-right motion on the water surface.

the surface temperature of the tail rapidly increases due to the Joule-heating effect, warming the surrounding water, which results in $T_1 > T_2$. A higher water temperature leads to a lower surface tension, i.e., $\gamma_1 < \gamma_2$. Therefore, the electrical-driven Marangoni actuator can move forward spontaneously. After applying a voltage of 3.7 V across the CNT-CF film for 2 s, its surface temperature increased to 59.4 °C (Fig. 3(a-iii)), confirming its rapid thermal response capability. Fig. 3(c) illustrates the directional movement process of the electrical-driven Marangoni actuator on the water surface. The trajectory reveals that the actuator advanced 68 mm within 13 s, with a deflection of less than 1.5 mm in the direction perpendicular to its forward motion (Fig. 3(d)). The complete motion process is provided in Movie S1 in the ESM. The moving velocity of the electrical-driven Marangoni actuator on the water surface was analyzed. The results indicate that the actuator had an average velocity of ~ 5.4 mm s^{-1} with a driving voltage of 3.7 V (Fig. 3(e)). The velocities of the Marangoni actuator with other driving voltages are shown in Fig. S7 in the ESM. The results indicate that a higher driving voltage leads to a higher average velocity of the electrical-driven Marangoni actuator. The deflection angle during the moving of actuator is defined as the angle between the vertical direction and the direction of the real-time position of the actuator relative to its initial position, with clockwise being positive and counterclockwise being negative. As shown in Fig. 3(f), the actuator exhibited a small real-time deflection angle (< 6°), further confirming its highly linear motion.

In addition, the electrical-driven Marangoni actuator can achieve diverse motion modes by controlling the localized heating position to create an asymmetric surface tension gradient. As presented in Fig. 4(a), applying a voltage to the CNT-CF films at positions 1, 2 and 3 on the tail of the Marangoni actuator can easily achieve turning-right, linear and turning-left motions (Fig. 4(b)). The dimensions for the Marangoni actuator are provided in Fig. S1(c) in the ESM. Notably, the power on/off of channels 1, 2 and 3 are controlled by a multi-channel wireless module, of which the optical photograph is shown in Fig. S8 in the ESM. Fig. 4(c-e) display optical photographs of the Marangoni actuator during turning-left, linear and turning-right motions respectively, as well as the corresponding device circuit schematics. This electrical-driven Marangoni actuator can precisely construct asymmetric temperature gradient fields via the Joule-heating effect, facilitating highly programmable linear and turning motions. The complete process of turning-left and turning-right motions are shown in Movie S2 and Movie S3 in the ESM. Notably, the precise control of the electrical-driven Marangoni robot is attributed to its excellent thermal response and cooling efficiency. As shown in Fig. S9(a) in the ESM, this electrical-driven Marangoni actuator can achieve a temperature change of ~40 °C within 2 s of both power-on and power-off. Furthermore, we tested the steering precision of the electrical-driven actuator during the turning-left motion (Fig. S9(b) in the ESM). It can be observed that after power-off, there is a certain time delay before the actuator stops moving, which is primarily caused by inertia. Furthermore, the real-time velocities during the turning-left and turning-right processes of the Marangoni actuator are shown in Fig. S10 in the ESM. Specifically, the average velocities for turning-left and turning-right motions of the Marangoni actuator were about 5.5 mm s^{-1} and 7.4 mm s^{-1}, respectively. Overall, such diverse motion modes give conventional Marangoni actuators the ability to meet path planning requirements in complex aquatic environments. For example, the actuators can navigate around surface obstacles in environmental monitoring scenarios and precisely adjust their direction for targeted delivery in micro-material transportation.

In addition to the electrical-driven motion achieved via the Marangoni effect (left panel of Fig. 5(a)), this Marangoni actuator can also be driven by chemical “fuel”, as shown in the middle panel of Fig. 5(a). The actuator mimics the behavior of some aquatic insects, such as rove beetles, which move freely on the water surface by secreting substances that reduce surface tension. Therefore, a piece of solid-state bone glue film was fixed underneath the tail of the Marangoni actuator. When the actuator touched the water surface, the bone glue gradually dissolved and diffused into the surroundings, forming a high-concentration area near the tail of the actuator. Generally, a higher concentration of bone glue results in a lower surface tension. Consequently, a surface tension gradient is created between the head and tail of the actuator. Due to the Marangoni effect, the actuator can undergo spontaneous directional motion. The velocity of chemical-driven Marangoni actuator during motion is shown in Fig. 5(b). The chemical-driven Marangoni actuator with the bone glue film (size of 2 cm × 1 cm) can accelerate to a stable velocity of ~11.3 mm s^{-1}, which is two times higher than that of the electrical-driven actuator. Furthermore, chemical-driven Marangoni actuators with other sizes of bone glue films (2 cm × 0.5 cm and 2 cm × 0.75 cm) achieve velocities of ~6.2 mm s^{-1} and ~8.9 mm s^{-1}, respectively (Fig. S11 in the ESM). These results demonstrate that a larger size of bone glue film leads to a higher velocity of the chemical-driven Marangoni actuator. The motion trajectory of the chemical-driven Marangoni actuator is shown in Fig. S12(a) in the ESM. Movie S4 in the ESM provides the complete motion process of the chemical-driven Marangoni actuator. Despite this, there remains room for improvement in terms of programmable motion and durability. Firstly, the diffusion of bone glue on the water surface is typically widespread and greatly affected by environmental factors such as water flow and temperature, which makes precise trajectory control difficult. Secondly, since this chemical-driven actuation mode relies on the continuous dissolution of bone glue, motion stops once the “fuel” is depleted or the concentration saturates, resulting in limited operational time.

To address the above issues, it is necessary to overcome the performance limitations of a single actuation mode and balance the conflict between solute diffusion and precise control. Interestingly, when driving a modern intelligent racing car, the driver can freely adjust the operating mode to meet their needs. For example, the E-Drive mode (i.e., pure electric) can reduce engine noise and lower “fuel” consumption. The performance mode (i.e., pure fuel) balances power output and “fuel” economy. The hybrid mode (i.e., SPORT+/RACE) enables the car to rapidly enter a “combat state”, maximizing its speed and providing an enjoyable driving experience. Inspired by the multi-mode propulsion strategies of racing cars, we present a novel dual-driven Marangoni actuator that combines electrical-driven and chemical-driven propulsion (right panel of Fig. 5(a)). This actuator not only incorporates the rapid capabilities of chemical-driven actuator, but also retains the precise controllability of electrical-driven actuator. Furthermore, the dual-driven mode is not merely a superposition, but rather achieves a coupling-enhancement effect through the synergy of the two modes. As illustrated in Fig. S12(b) in the ESM, the dual-driven Marangoni actuator can move 136 mm forward within 5 s, as demonstrated in Movie S5 in the ESM. The real-time velocity of the dual-driven Marangoni actuator is shown in Fig. 5(c). The results indicate that the average velocity of the dual-driven Marangoni actuator is ~32.2 mm s^{-1} (Fig. 5(d)), surpassing the arithmetic sum values of pure electrical-driven (5.4 mm s^{-1}) and pure chemical-driven (11.3 mm s^{-1}) actuators (32.2 > 5.4 + 11.3). Notably, this dual-driven Marangoni actuator offers significant advantages compared to previous reports on advanced Marangoni actuators, particularly in terms of velocity and controllability (Table S1 in the ESM). We consider the electrical-chemical synergistic enhancement effect to be primarily attributed to the higher surface temperature and “fuel” concentration, which increase the surface tension gradient across the ends of the actuator. Moreover, the Joule-heating effect induced by electrical-driven speeds up the dissolution rate of the bone glue film, which further boosts the surface tension gradient. As illustrated in Fig. S13 in the ESM, the dissolution rate of the bone glue film in water at 65 °C is nearly four times higher than that in water at 25 °C. More details are described in the Experimental Section.

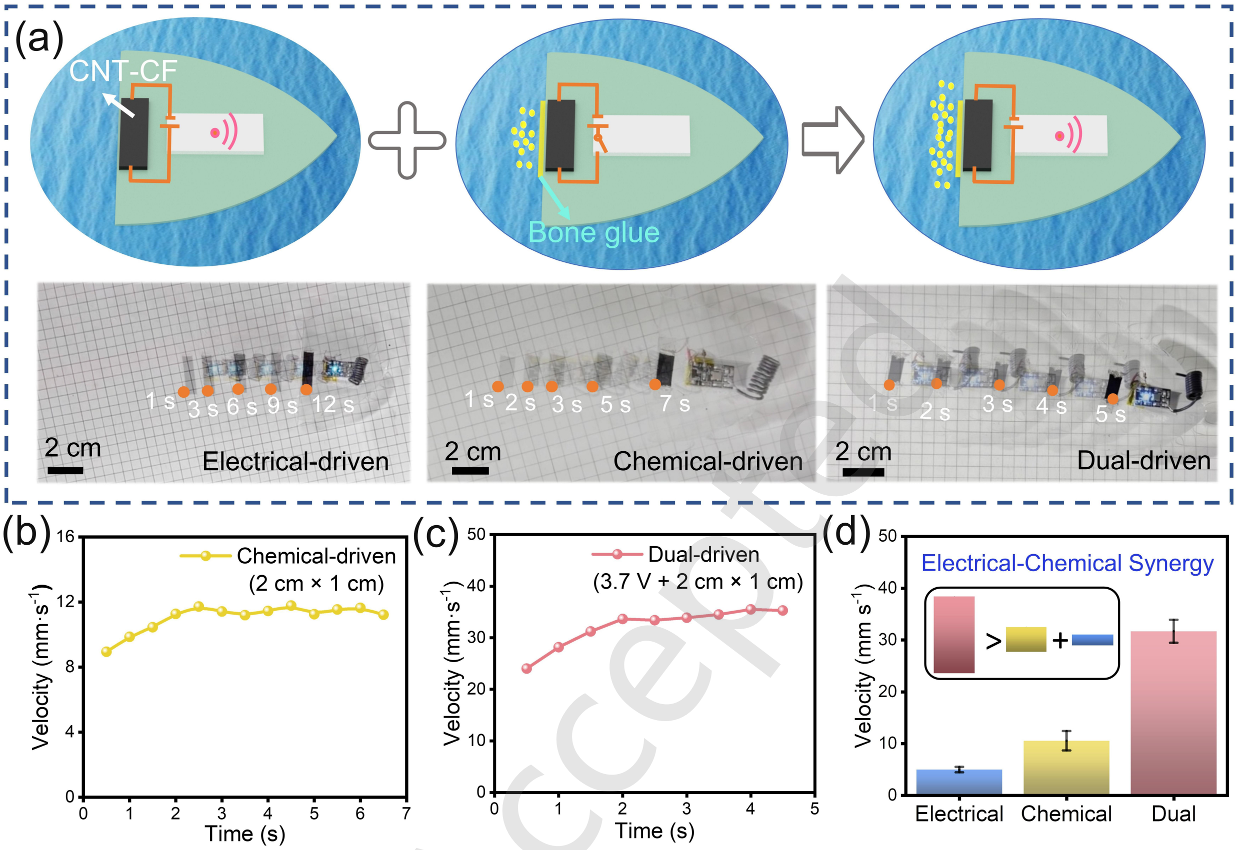

Figure 5 (a) Schematic diagrams and corresponding photographs of the motion trajectories of electrical-driven, chemical-driven and dual-driven Marangoni actuators, inspired by the multimode motion of racing car (electricity, fuel and hybrid). (b) Velocity of the chemical-driven Marangoni actuator as a function of time with the bone glue film (size of 2 cm × 1 cm). (c) Velocity of the dual-driven Marangoni actuator as a function of time with the driving voltage of 3.7 V and bone glue film (size of 2 cm × 1 cm). (d) Average velocities of the electrical-driven, chemical-driven and dual-driven Marangoni actuators.

The CNT-CF/PE composite material system not only has applications in the fabrication of on-water Marangoni actuators and swimming robots, but can also serve as a “one material, multiple uses” solution for constructing actuators that can deform on the land. Based on the bilayer structure of CNT-CF and PE composite films, an electrical-driven crawling CNT-CF/PE actuator was designed with dimensions of 5 cm × 1 cm (Fig. S14 in the ESM). As shown in Fig. 6(a), this actuator can mimic the crawling motion of an inchworm. The complete crawling process of the actuator on a ratchet substrate is provided in Movie S6 in the ESM. Specifically, when a voltage is applied to two ends of the CNT-CF/PE composite film, the CNT-CF side heats up rapidly due to the Joule-heating effect, heating the PE layer as well. The CTE of CNT is very small [38], which is two orders of magnitude smaller than that of PE [39, 40]. Consequently, the volume mismatch caused by the difference in CTE results in the CNT-CF/PE composite film bending towards the CNT-CF side. Moreover, the deformation amplitude increases with longer voltage-on time. When the voltage was turned off, the actuator gradually returned to its initial state as the temperature decreased.

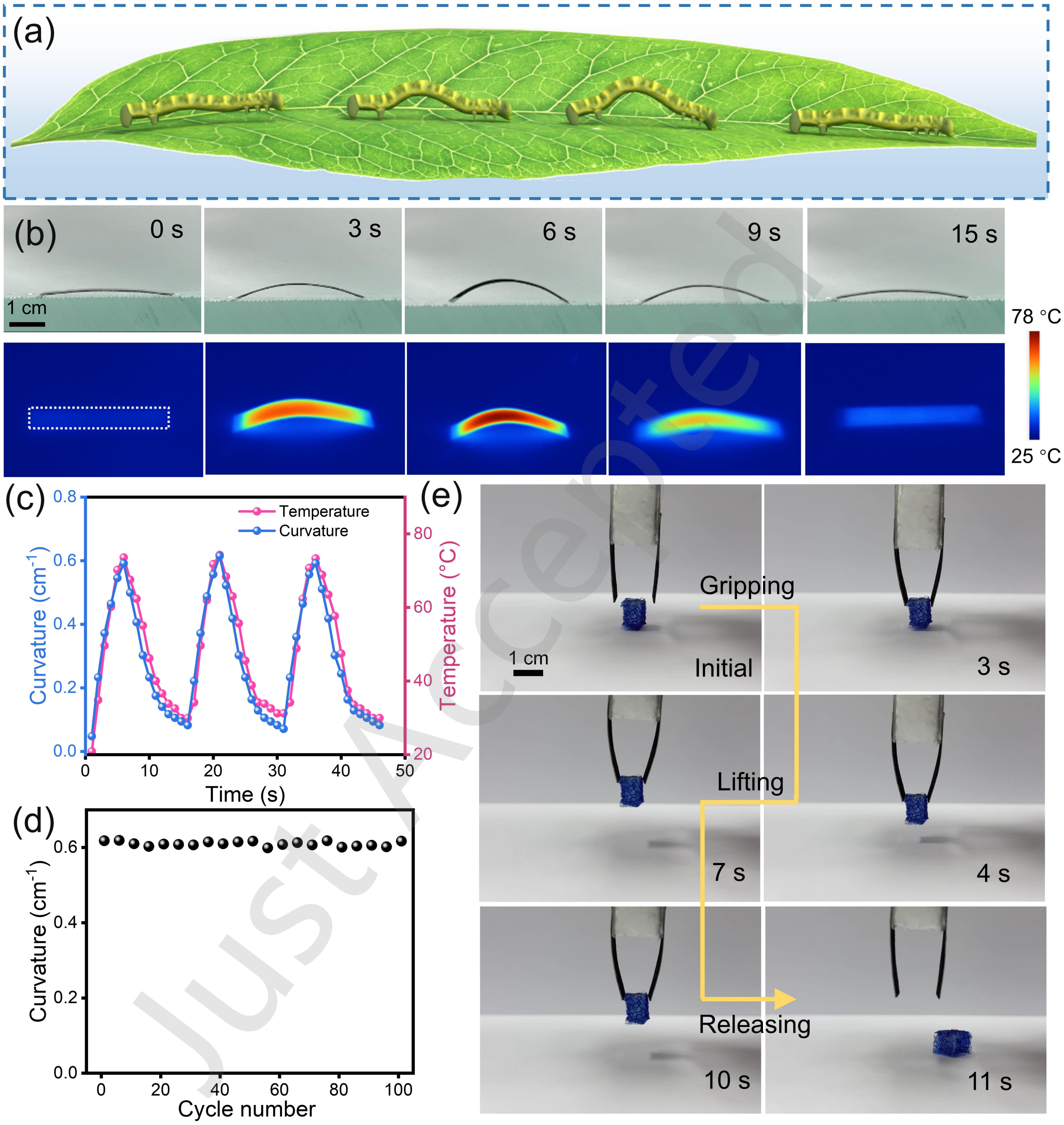

Figure 6 (a) Schematic diagram of an inchworm crawling. (b) Optical photographs and corresponding infrared images of the CNT-CF/PE actuator during one crawling cycle under a voltage of 5 V. (c) Bending curvature and surface temperature of the CNT-CF/PE actuator as a function of time over three crawling cycles. (d) Maximum bending curvature of the CNT-CF/PE actuator over 100 cycles. (e) Optical photographs showing the entire process of an electrical-driven robotic gripper based on the CNT-CF/PE actuators for gripping and releasing an object.

Fig. 6(b) displays optical photographs of a single actuation cycle and the corresponding infrared images. The real-time bending curvature and surface temperature of the CNT-CF/PE actuator during three deformation cycles are presented in Fig. 6(c). It can be observed that they exhibit a high degree of synchronization. Specifically, applying a voltage of 5 V to the CNT-CF/PE actuator for 5 s results in a maximum temperature of ~72 °C. Meanwhile, the maximum bending curvature of the composite film is ~ 0.61 cm^{-1}. The relevant parameters and calculation process for the bending curvature are provided in Fig. S15 in the ESM and Note S2 in the ESM. Furthermore, cycling stability is an important parameter for evaluating the long-term operational potential of an actuator. As illustrated in Fig. 6(d), the maximum bending curvature of the actuator did not decrease significantly over 100 cycles.

To further verify the multifunctionality of this CNT-CF/PE composite in the field of bionics, we constructed an electrical-driven robotic gripper using two U-shaped CNT-

CF/PE actuators with dimensions of 3 cm × 1 cm (Fig. S16 in the ESM). When a voltage was applied to the two actuators, the gripper gradually closed to grasp an object. With continued power supply, the object can be lifted up. When the voltage was turned off, the gripper gradually opened to release the object (Fig. 6(e)). Notably, the weight of the object was ~ 0.11 g. The complete process is presented in Movie S7 in the ESM. This gripper showcases its potential in applications such as micro-assembly robotics and bionic robotic arms.

4 Conclusions

In summary, we successfully develop a Marangoni actuator that couples electrical and chemical actuation by combining CNT-CF composite film with PE film. Through a streamlined asymmetric structural design, this actuator can execute diverse motion modes on water surfaces, including programmable linear and turning trajectories via the electrical-driven Marangoni effect. The actuator also achieves rapid propulsion by means of the chemical-driven Marangoni effect triggered by dissolution of an embedded bone glue film. Notably, a synergistic dual-driven strategy that couples both electrical and chemical stimuli enable the actuator to attain an impressive velocity of 32.2 mm s^{-1}, surpassing the arithmetic sum velocities of its individual actuation modes by over 93%. Furthermore, leveraging the volume mismatch effect caused by the difference in CTE between the CNT-CF composite and the PE film, the same CNT-CF/PE materials system can be designed as actuators that can mimic inchworm on-land crawling motions, and assembled into a robotic gripper, showcasing the "one material, multiple uses" characteristic of the CNT-CF/PE composite material. This multifunctional composite material is expected to have significant potential applications in fields such as soft robotics and amphibious devices.

Electronic Supplementary Material: Supplementary material (characterization, supporting note: calculation of conductivity, calculation of the bending curvature. Figures: schematic diagram of the dimensions for the bullet-shaped PE film, linear motion electrical-driven Marangoni actuator, turning motion electrical-driven Marangoni actuator and dual-driven Marangoni actuator, SEM images of CNT-CF (1:1), CNT-CF (2:1), CNT-CF (3:1), CNT-CF (5:1) films at different magnifications, surface temperature of CNT-CF (1:1), CNT-CF (2:1), CNT-CF (3:1), CNT-CF (4:1) and CNT-CF (5:1) as a function of time, comparison of the conductivity, heating rate, Young's modulus, toughness, and breaking strain properties of CNT-CF composites with different ratios, optical photos of the linear motion electrical-driven Marangoni actuator, the whole process of charging the micro-power supply, velocities of the electrical-driven Marangoni actuator under different driving voltages, optical photo of the multi-channel wireless control module, temperature and angular velocity of the Marangoni actuator on the water when driven by a voltage of 3.7 V, velocities of the electrical-driven Marangoni actuator as a function of time during turning-left and turning-right motions, velocities of the chemical-driven Marangoni actuator with the various sizes of bone glue films, trajectory of chemical-driven and dual-driven Marangoni actuator, dissolution rate of the bone glue film under various water temperatures, optical photo of the strip-shaped CNT-CF/PE actuator, the parameters of the bending curvature calculation, optical photo of a U-shaped CNT-CF/PE actuator. Table: comparison of the comprehensive performance of other reported Marangoni actuators. Movie: linear, turning-left, and turning-right motions of the electrical-driven Marangoni actuators, motions of chemical-driven and dual-driven Marangoni actuators, a crawling actuator, a robotic gripper) is available in the online version of this article at https://doi.org/10.26599/NR.2026.94908831.

Data availability

All data needed to support the conclusions in the paper are presented in the manuscript and the Electronic Supplementary Material. Additional data related to this paper may be requested from the corresponding author upon request.

Acknowledgements

This work is supported by the National Natural Science Foundation of China (Grant Nos. 52373113, 51773039), Natural Science Foundation of Fujian Province (Grant Nos. 2025J02017, 2025J08242, 2020J02036), Top Young Talents Program of Fujian Province, Startup Fund for Advanced Talents of Putian University (Grant No. 2024040), and Putian Municipal Science and Technology Program Projects (Grant No. 2025SZ3001PTXY04).

Declaration of competing interest

All the contributing authors report no conflict of interests in this.

Author contribution statement

Y.C.: Investigation, writing-original draft, data curation, visualization. Y.Q.: Investigation, formal analysis, funding acquisition, writing-original draft. W.Z.: validation, project administration, writing-review & editing. Z.L.: Investigation, validation, writing-review & editing. L.C.: Conceptualization, funding acquisition, writing-review & editing, resources, supervision. All the authors have approved the final manuscript.

Use of AI statement

None.

References

[1] Wang, Q.; Sun, H.; Zou, C.; Chen, C. Photo-, Thermal-, and electro-responsive polyolefin-based actuators. *Angew. Chem., Int. Ed.* **2026**, *65*, e23449.

[2] Zeng, L.; Chen, L.; Lin, J.; Lin, J.; Wu, Y.; Wang, Y.; Luo, Z.; Huang, F.; Chen, D. Glow-worm-inspired fluorescent self-healing actuators for soft robot and reconfigurable information encryption. *Adv. Mater.* **2025**, *37*, 2501007.

[3] Yu, H.; Wang, Y.; Hou, Z.; Xia, X.; Chen, H.; Zou, B.; Zhang, Y. Marangoni effect enabling autonomously miniatured swimmers: mechanisms, design strategy, and applications. *Adv. Funct. Mater.* **2025**, *35*, 2424235.

[4] Weng, M.; Zhou, J.; Zhou, P.; Shang, R.; You, M.; Shen, G.; Chen, H. Multi-functional actuators made with biomass-based graphene-polymer films for intelligent gesture recognition and multi-mode self-powered

sensing. *Adv. Sci.* **2024**, *11*, 2309846.

[5] Wang, M.; Zhou, L.; Deng, W.; Hou, Y.; He, W.; Yu, L.; Sun, H.; Ren, L.; Hou, X. Ultrafast response and programmable locomotion of liquid/vapor/light-driven soft multifunctional actuators. *ACS Nano* **2022**, *16*, 2672-2681.

[6] Chen, H.; Xu, L.; Li, P.; Chen, Z.; Xiong, J.; Liu, Z.; Yan, Q.; Zheng, H.; Zhao, X.; Xue, F.; Lian, H.; Chen, Y.; Fei, T.; Hu, Y.; Peng, Q.; He, X. A self-sensing photoactuator based on temperature self-compensated MXene/graphite composite ink for objects recognition and biomimetic soft robotics. *Nano Res.* **2025**, *18*, 94907744.

[7] Fonseca, D.; Neto, P. Electrically-driven phase transition actuators to power soft robot designs. Nat. Commun. 2025, 16, 3920.

[8] Tang, Y.; Li, M.; Wang, T.; Dong, X.; Hu, W.; Sitti, M. Wireless miniature magnetic phase-change soft actuators. *Adv. Mater.* **2022**, *34*, 2204185.

[9] Zeng, S.; Ye, Y.; Zhou, P.; Yi, S.; Guo, Q.; Chen, H.; Shen, G.; Weng, M. Programmable and reconfigurable humidity-driven actuators made with MXene ($Ti_3C_2T_x$)-cellulose nanofiber composites for biomimetic applications. *Nano Res.* **2024**, *17*, 6619-6629.

[10] Yang, Y.; Wang, H.; Zhang, S.; Wei, Y.; He, X.; Wang, J.; Zhang, Y.; Ji, Y. Vitrimer-based soft actuators with multiple responsiveness and self-healing ability triggered by multiple stimuli. *Matter* **2021**, *4*, 3354-3365.

[11] Zhang, L.; Chen, L.; Xu, L.; Zhao, H.; Wen, R.; Xia, F. Gastrointestinal-peristalsis-inspired hydrogel actuators for NIR-controlled transport of viscous liquids. *Adv. Mater.* **2023**, *35*, 2212149.

[12] Cheng, Z.; Hua, Y.; Zhang, D.; Wang, M.; Ge, X.; Shen, Y.; Zhao, B.; Qi, N.; Lin, H. Bilayer oriented nanofiber membrane for enhancing response deformation and stability of humidity-responsive actuator. *Chem. Eng. J.* **2025**, *506*, 160260.

[13] Kim, M.; Heo, J.; Rodrigue, H.; Lee, H.; Pané, S.; Han, M.; Ahn, S. Shape memory alloy (SMA) actuators: the role of material, form, and scaling effects. *Adv. Mater.* **2023**, *35*, 2208517.

[14] Miao, J.; Zhang, T.; Li, G.; Guo, D.; Sun, S.; Tan, R.; Shi, J.; Shen, Y. Flagellar/ciliary intrinsic driven mechanism inspired all-in-one tubular robotic actuator. *Engineering* **2023**, *23*, 170-180.

[15] Yu, W.; Chen, W.; Yuan, W.; Li, G.; Meng, C.; Guo, S. Ultrathin and highly-stable rubber electrodes based on island-bridge multi-filler conductive network for multilayer-stacked dielectric elastomer artificial muscles. *Chem. Eng. J.* **2024**, *493*, 152714.

[16] Liu, R.; Li, Z.; Zhao, H.; Zhang, L.; Lan, R.; Wang, Q.; Yang, H. Dual-stimuli-responsive covalent organic framework-liquid crystal polymer smart actuator. *Adv. Funct. Mater.* **2025**, *35*, 2418627.

[17] Hu, Y.; Ji, Q.; Huang, M.; Chang, L.; Zhang, C.; Wu, G.; Zi, B.; Bao, N.; Chen, W.; Wu, Y. Light-driven self-oscillating actuators with phototactic locomotion based on black phosphorus heterostructure. *Angew. Chem., Int. Ed.* **2021**, *60*, 20511-20517.

[18] Wang, W.; Shao, W.; Li, N.; Guo, H.; Zeng, S.; Zhang, Y.; Zhang, J.; Han, D.; Zhang, Y. Graphene oxide foam-based floating actuators manipulated via dual-Marangoni-effect propulsion and magnetic-field-guided navigation. *Small Methods* **2025**, *9*, 2401946.

[19] Wang, W.; Han, B.; Zhang, Y.; Li, Q.; Zhang, Y.; Han, D.; Sun, H. Laser-induced graphene tapes as origami and stick-on labels for photothermal manipulation via Marangoni effect. *Adv. Funct. Mater.* **2021**, *31*, 2006179.

[20] Zhang, Z.; Gao, N.; Zhang, F.; Liu, L.; Chen, Y. Photothermal-driven water-gliding microrobots based on fully integrated flexible sensors with heterogeneous wettability. *Soft Science* **2025**, *5*, 15.

[21] Zhou, J.; Zhang, Y.; Zhang, M.; Yang, D.; Huang, W.; Zheng, A.; Cao, L. High-performance MXene hydrogel for self-propelled Marangoni swimmers and water-enabled electricity generator. *Adv. Sci.* **2025**, *12*, 2408161.

[22] Hou, K.; Zhao, P.; Li, C. A Light-driven actuator enables versatile motion for smart transportation and contactless delivery. *Adv. Opt. Mater.* **2023**, *11*, 2202949.

[23] Zhang, S.; Kwak, B.; Zhu, R.; Pankhurst, M.; Zhang, L.; Boom, R. M.; Floreano, D. Edible aquatic robots with Marangoni propulsion. *Nat. Commun.* **2025**, *16*, 4238.

[24] Mao, J.; Han, D.; Zhou, H.; Sun, H.; Zhang, Y. Bioinspired superhydrophobic swimming robots with embedded microfluidic networks and photothermal switch for controllable Marangoni propulsion. *Adv. Funct. Mater.* **2023**, *33*, 2208677.

[25] Zhou, Y.; Guan, X.; Zhao, D.; Zhang, K.; Huang, Y.; Zhong, J. Bio-inspired and programmable Marangoni motor for highly maneuverable and adaptable S-aquabots. *eScience* **2025**, *5*, 100335.

[26] Chen, Z.; Zhao, X.; Gao, B.; Xu, L.; Chen, H.; Liu, Z.; Li, P.; Yan, Q.; Zheng, H.; Xue, F.; Xiong, J.; Ding, R.; Fei, T.; Tang, Z.; Peng, Q.; Hu, Y.; He, X. Biobased inks based on cuttlefish ink and cellulose nanofibers for biodegradable patterned soft actuators. *ACS Appl. Mater. Interfaces* **2024**, *16*, 22547-22557.

[27] Tang, J.; Xi, K.; Chen, H.; Wang, L.; Li, D.; Xu, Y.; Xin, T.; Wu, L.; Zhou, Y.; Bian, J.; Cai, Z.; Yang, H.; Deng, L.; Gu, Y.; Cui, W.; Chen, L. Flexible osteogenic glue as an all-in-one solution to assist fracture fixation and healing. *Adv. Funct. Mater.* **2021**, *31*, 2102465.

[28] Qian, L.; Xie, Y.; Zou, M.; Zhang, J. Building a bridge for carbon nanotubes from nanoscale structure to macroscopic application. *J. Am. Chem. Soc.* **2021**, *143*, 18805-18819.

[29] Yang, Y.; Wu, Y.; Liu, C.; Hambsch, M.; Dong, T.; Bodesheim, D.; Prasad, M.; Dianat, A.; Kühne, T. D.; Cuniberti, G.; Mannsfeld, S. C. B.; Parkin, S. S. P.; Dong, R.; Wang, Z.; Feng, X. On-liquid surface synthesis of diyne-linked two-dimensional polymer crystals. *Nat. Commun.* **2025**, *16*, 8243.

[30] Han, X.; Hao, C.; Peng, Y.; Yu, H.; Zhang, T.; Zhang, H.; Chen, K.; Chen, H.; Wang, Z.; Yan, N.; Pu, J. Novel cellulosic fiber composites with integrated multi-band electromagnetic interference shielding and energy storage functionalities. *Nano-Micro Lett.* **2025**, *17*, 122.

[31] Liu, Y.; Zhang, S.; Li, L.; Li, N. High-performance cellulose nanofibers/carbon nanotubes composite for constructing multifunctional sensors and wearable electronics. *Adv. Fiber Mater.* **2024**, *6*, 758-771.

[32] Cao, W.; Ma, C.; Tan, S.; Ma, M.; Wan, P.; Chen, F. Ultrathin and flexible CNTs/MXene/cellulose nanofibrils composite paper for electromagnetic interference shielding. *Nano-Micro Lett.* **2019**, *11*, 72.

[33] Yuan, Z.; Meng, D.; Wu, Y.; Tang, G.; Liang, P.; Xin, J. H.; Ye, D. Raman imaging-assisted customizable assembly of MOFs on cellulose aerogel. *Nano Res.* **2022**, *15*, 2599-2607.

[34] Salem, K. S.; Kasera, N. K.; Rahman, M. A.; Jameel, H.; Habibi, Y.; Eichhorn, S. J.; French, A. D.; Pal, L.; Lucia, L. A. Comparison and assessment of methods for cellulose crystallinity determination. *Chem. Soc. Rev.* **2023**, *52*, 6417-6446.

[35] Sacui, I. A.; Nieuwendaal, R. C.; Burnett, D. J.; Stranick, S. J.; Jorfi, M.; Weder, C.; Foster, E. J.; Olsson, R. T.; Gilman, J. W. Comparison of the properties of cellulose nanocrystals and cellulose nanofibrils isolated from bacteria, tunicate, and wood processed using acid, enzymatic, mechanical, and oxidative methods. *ACS Appl. Mater. Interfaces* **2014**, *6*, 6127-6138.

[36] Zhang, P.; Fan, J.; Wang, Y.; Dang, Y.; Heumann, S.; Ding, Y. Insights into the role of defects on the Raman spectroscopy of carbon nanotube and biomass-derived carbon. *Carbon* **2024**, *222*, 118998.

[37] Quan, G.; Wu, Y.; Li, W.; Li, D.; Liu, X.; Wang, K.; Dai, S.; Xiao, L.;

Ao, Y. Construction of cellulose nanofiber/carbon nanotube synergistic network on carbon fiber surface to enhance mechanical properties and thermal conductivity of composites. *Compos. Sci. Technol.* **2024**, *248*, 110454.

[38] Zhu, Z.; Li, K.; Hao, X.; Dai, X.; Wang, J.; Yin, F.; Wang, H. Rollable single-piece thermoelectric generators at cryogenic temperature fabricated with high-performance CNT films achieved by doping modulation. *Adv. Sci.* **2026**, *13*, e15688.

[39] Wu, F.; Lin, X.; Xu, Y.; Zhang, D.; He, Y.; Liu, M. Light-driven locomotive soft actuator and multi-functional sensors based on asymmetric PVA/carbon/PE bilayer film. *Sci. China Mater.* **2023**, *66*, 4782-4793.

[40] Sheng, S.; Xian, Z.; Zhang, W.; Wang, J.; Feng, X.; Pei, G.; Zhao, B.; Liu, J.; Yu, S. Smart curtains for spontaneous solar modulation via natural light-triggered deformable shading and chromogenic synergy. *Adv. Mater.* **2026**, *38*, e10042

Electronic Supplementary Material

Racing-car-inspired electrical/chemical dual-driven actuators for swimming Marangoni robots based on carbon nanotube composites

Yuhang Chen[1,2,§], Yongqiang Qian[3,§,], Wei Zhang[1,2], Zhiling Luo[1,2,], and Luzhuo Chen[1,2,]

[1] Fujian Provincial Key Laboratory of Quantum Manipulation and New Energy Materials, College of Physics and Energy, Fujian Normal University, Fuzhou, 350117, China
[2] Fujian Provincial Engineering Technology Research Center of Solar Energy Conversion and Energy Storage, Fujian Normal University, Fuzhou, 350117, China
[3] Fujian Laser Precision Machining Engineering Technology Research Center, College of Intelligent Manufacturing, Putian University, Putian, 351100, China
[§] Yuhang Chen and Yongqiang Qian contributed equally to this work.

Supporting information to https://doi.org/10.26599/NR.2026.94908831

Characterization

The microstructure of the samples was observed using field-emission scanning electron microscopy (SU8010, Hitachi). Crystal structure was analyzed by X-ray diffraction (Rigaku SmartLab SE). Raman spectra were recorded using a Raman spectrometer (HR Evolution, HORIBA) with an excitation wavelength of 532 nm. The electrical properties of the samples were analyzed using an electrochemical workstation (CHI 660E). The mechanical properties of the samples were tested using a material testing machine (Instron 3343). Temperature acquisition was conducted using a laser thermometer (Optris LS). Open-circuit voltage was measured using a digital multimeter (UNI-T UT33B+). The crawling and gripping functions of the CNT-CF composite film were tested using a DC regulated power supply (WANPTEK GPS305D). Infrared images were recorded using an infrared thermal camera (Fluke Ti10). Optical photographs and movies were captured using an iPhone 16 Pro.

Supporting Note

Note S1 Calculation the conductivity of CNT-CF composites

The resistance of the CNT-CF composites at room temperature is defined by

$$R = \frac{\rho L}{S}. \tag{S1}$$

Therefore, the resistivity can be derived by

$$\rho = \frac{RS}{L} = Rd, \tag{S2}$$

where R represents the square resistance, L represents the length, S represents the cross-sectional area, and d represents the thickness.

The conductivity (σ) is defined as the reciprocal of the resistivity, given by

$$\sigma = \frac{1}{\rho} = \frac{1}{Rd}. \tag{S3}$$

Address correspondence to Yongqiang Qian, qianyongqiang@ptu.edu.cn; Zhiling Luo, luozl@fjnu.edu.cn; Luzhuo Chen, ChenLZ@fjnu.edu.cn

Note S2 Calculation of the bending curvature of CNT-CF/PE composites

In this work, parameters are defined as follows:

h represents the height of the CNT-CF/PE composite from the ground. represents the radius of the circle on which the CNT-CF/PE composite lies. represents half the chord length in contact with the ground for the CNT-CF/PE composite, as shown in Fig. S15 in the ESM.

Based on trigonometric relationships, the following is evident:

$$(r-h)^2+d^2=r^2. \tag{S4}$$

The can be calculated by

$$r=\frac{h^2+d^2}{2h}. \tag{S5}$$

Thus, the bending curvature $(\frac{1}{r})$ can be expressed as

$$\frac{1}{r}=\frac{2h}{h^2+d^2}. \tag{S6}$$

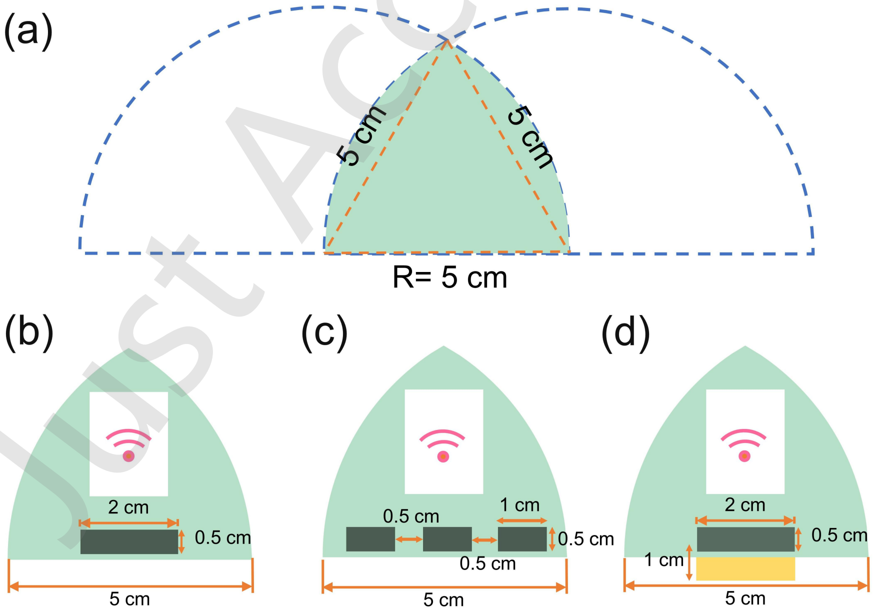

Figure S1 (a) Schematic diagram of the dimensions for the bullet-shaped PE film. (b) Schematic diagram of the dimensions of the linear motion electrical-driven Marangoni actuator. (c) Schematic diagram of the dimensions of the turning motion electrical-driven Marangoni actuator. (d) Schematic diagram of the dimensions of the dual-driven Marangoni actuator.

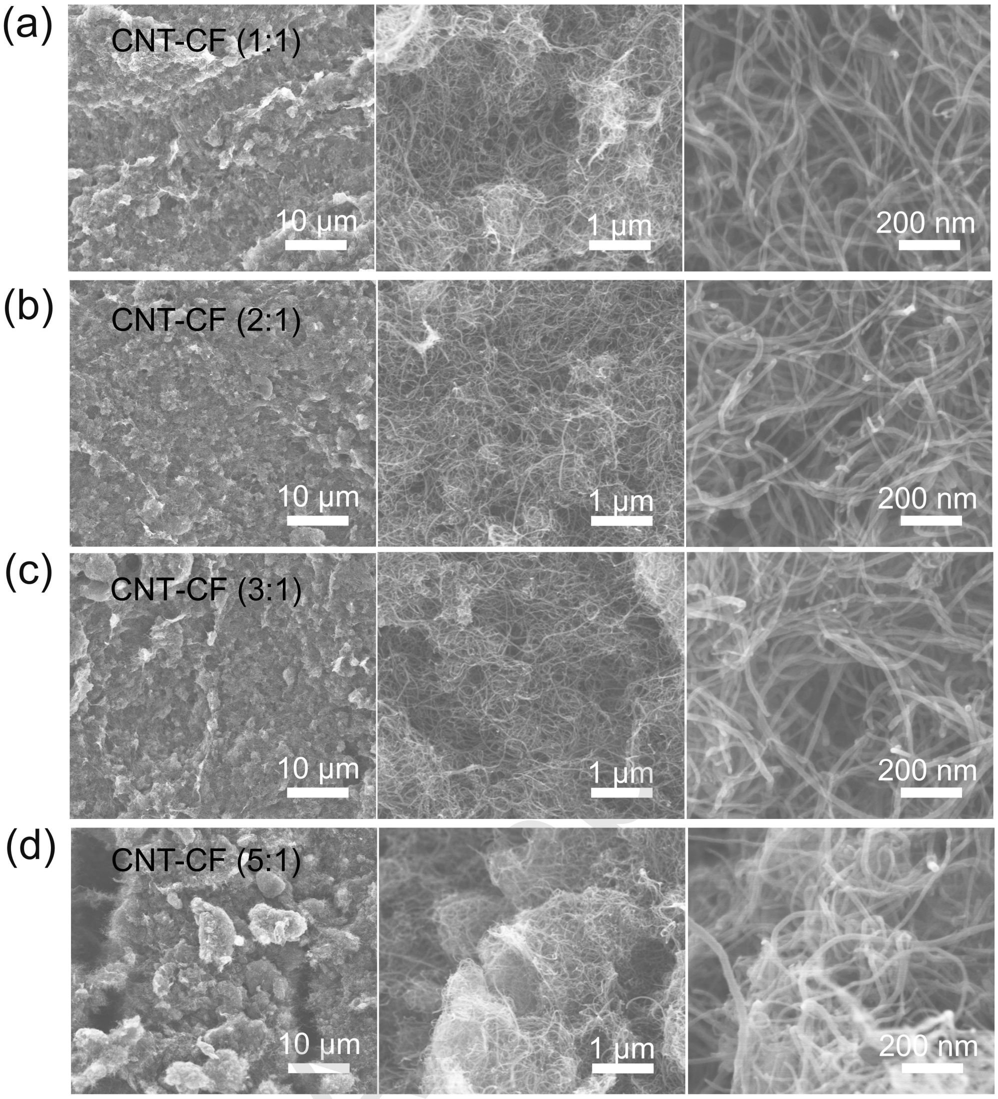

Figure S2 (a) SEM images of CNT-CF (1:1) film at different magnifications. (b) SEM images of CNT-CF (2:1) film at different magnifications. (c) SEM images of CNT-CF (3:1) film at different magnifications. (d) SEM images of CNT-CF (5:1) film at different magnifications.

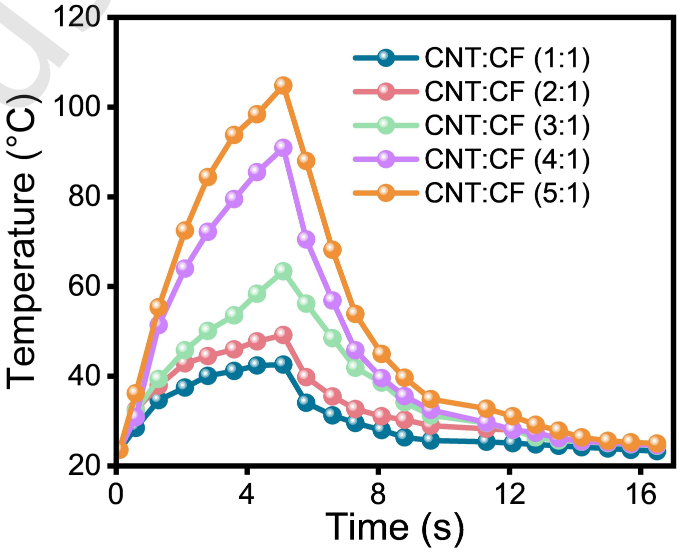

Figure S3 Surface temperature of CNT-CF (1:1), CNT-CF (2:1), CNT-CF (3:1), CNT-CF (4:1) and CNT-CF (5:1) as a function of time with applied voltage of 3.7 V for 5 s.

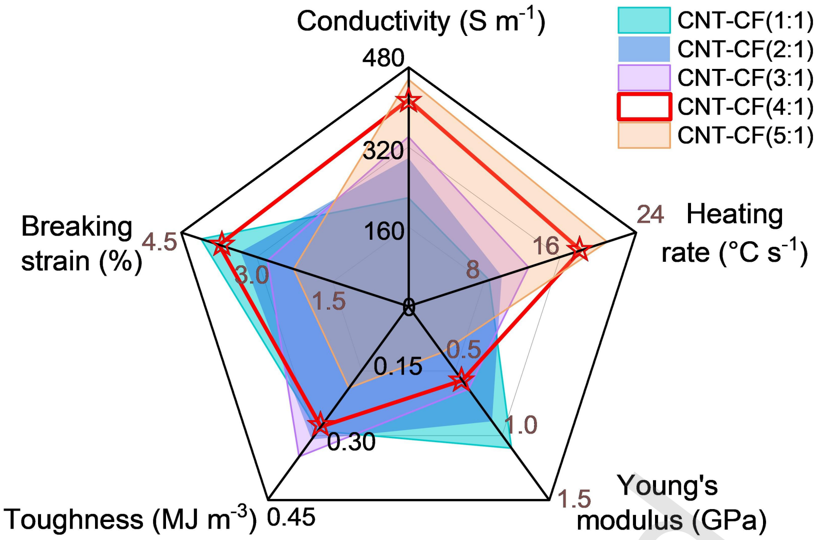

Figure S4 Comparison of the conductivity, heating rate, Young's modulus, toughness, and breaking strain properties of CNT-CF composites with different ratios.

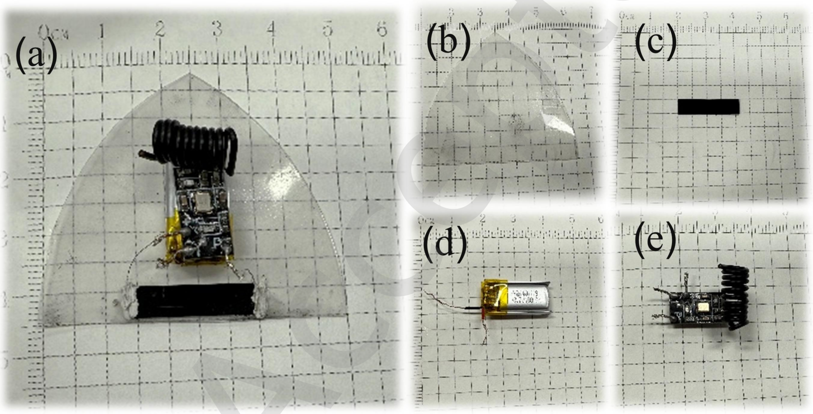

Figure S5 (a) Optical photograph of the linear motion electrical-driven Marangoni actuator. (b) Bullet-shaped PE film. (c) CNT-CF film. (d) Micro-power supply. (e) Wireless module.

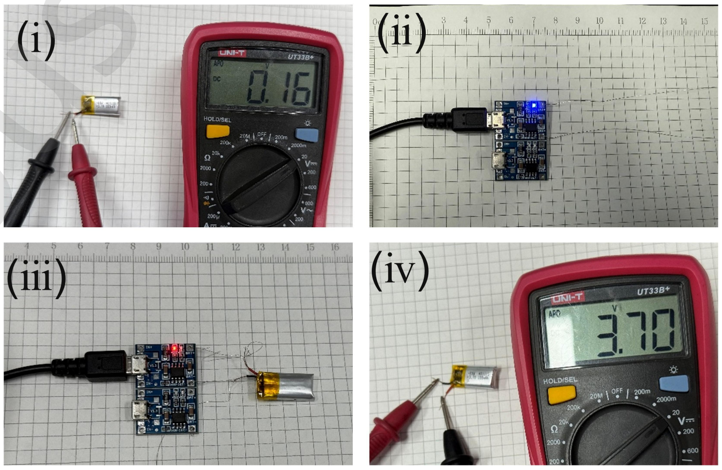

Figure S6 The whole process of charging the micro-power supply, which can be charged by connecting to a power source via a USB charging cable.

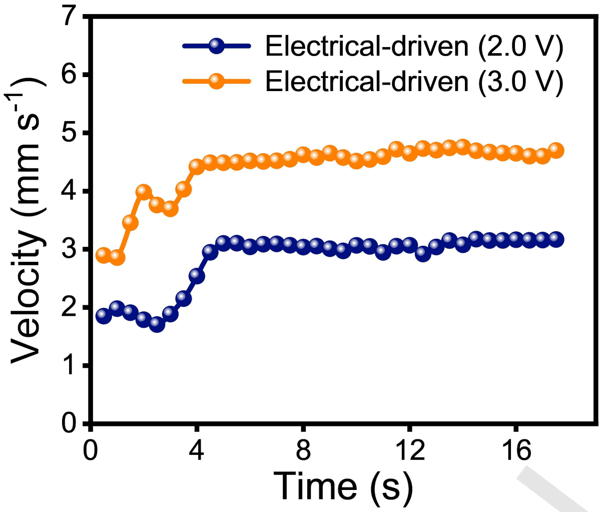

Figure S7 Velocities of the electrical-driven Marangoni actuator as a function of time under the driving voltages of 2 V and 3 V.

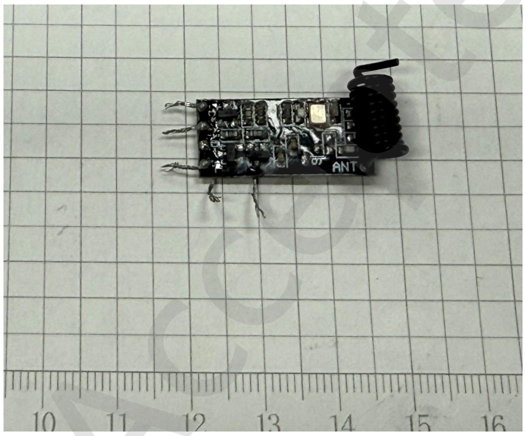

Figure S8 Optical photograph of the multi-channel wireless control module.

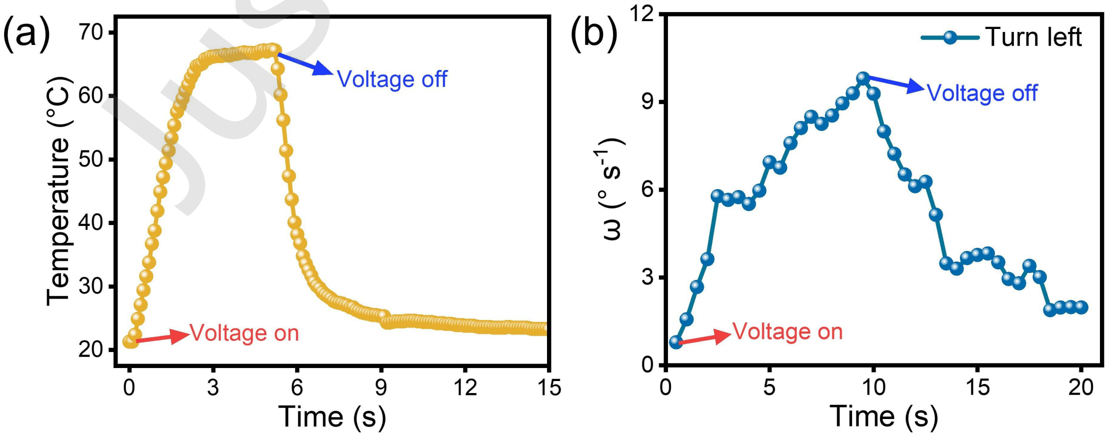

Figure S9 (a) Temperature of the electrical-driven Marangoni actuator on the water when driven by a voltage of 3.7 V. (b) Angular velocity of the electrical-driven Marangoni actuator during turning-left motion when driven by a voltage of 3.7 V.

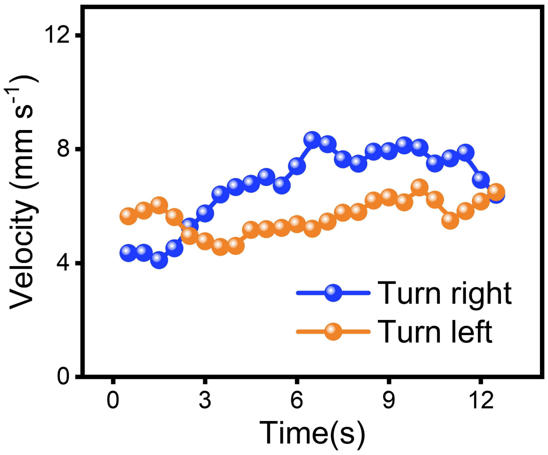

Figure S10 Velocities of the electrical-driven Marangoni actuator as a function of time during turning-left and turning-right motions.

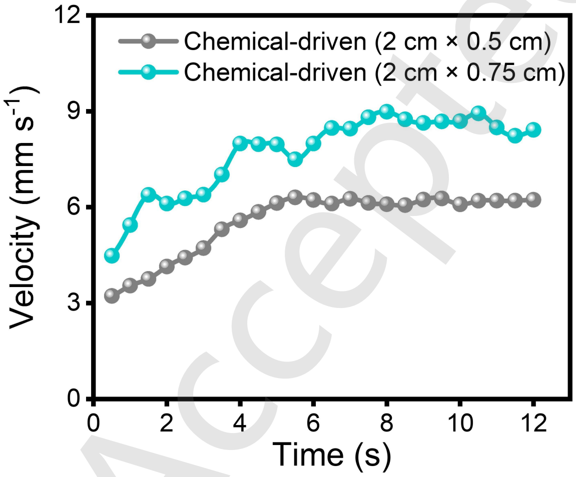

Figure S11 Velocities of the chemical-driven Marangoni actuator as a function of time with other sizes of bone glue films (2 cm × 0.5 cm and 2 cm × 0.75 cm).

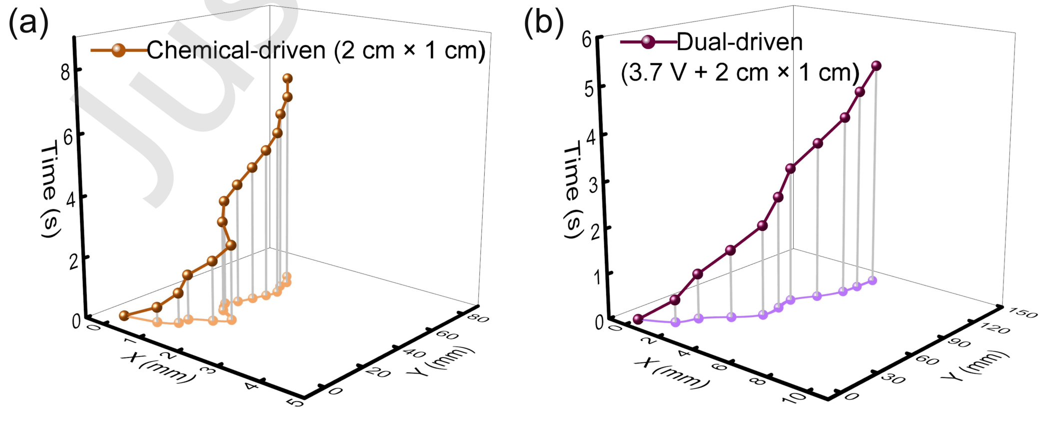

Figure S12 (a) Trajectory of chemical-driven Marangoni actuator with the bone glue film (size of 2 cm × 1 cm). (b) Trajectory of the dual-driven Marangoni actuator with the driving voltage of 3.7 V and bone glue film (size of 2 cm × 1 cm).

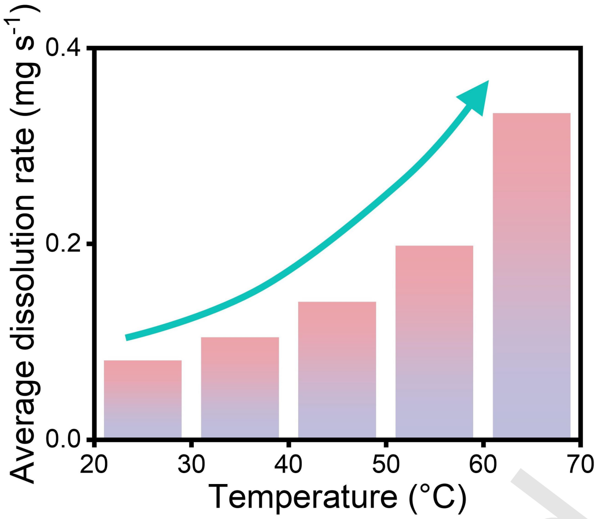

Figure S13 Dissolution rate of the bone glue film as a function of water temperature.

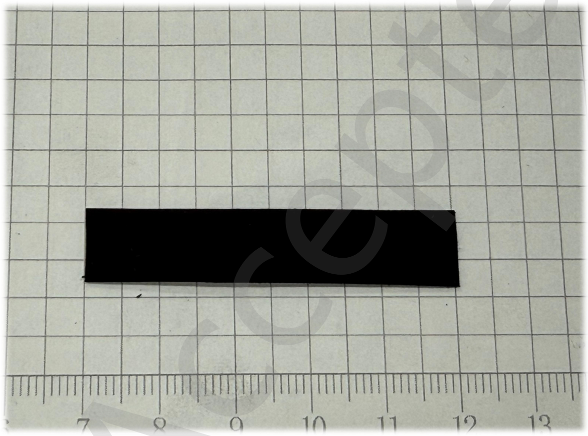

Figure S14 Optical photograph of the strip-shaped CNT-CF/PE actuator.

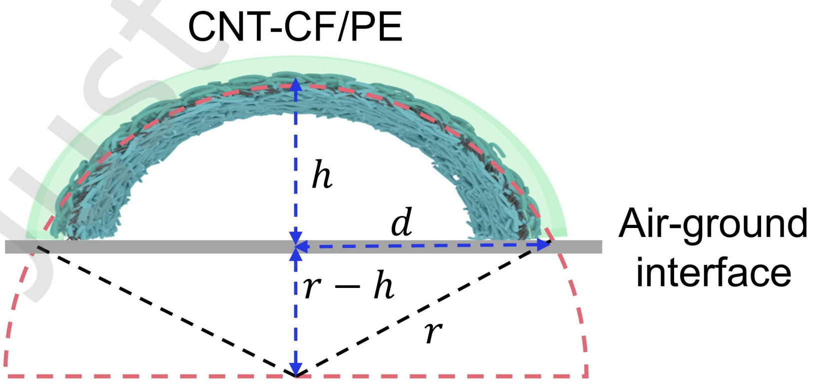

Figure S15 The parameters of the bending curvature calculation during the crawling process for the CNT-CF/PE composite film.

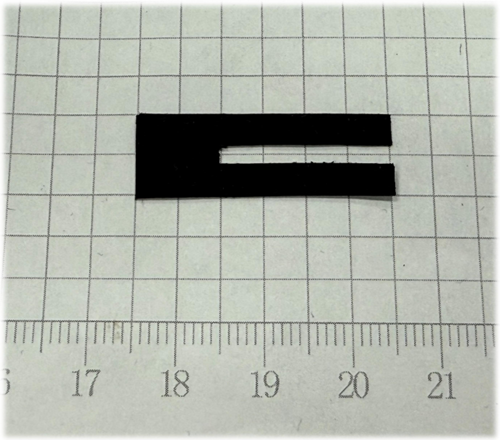

Figure S16 Optical photograph of a U-shaped CNT-CF/PE composite film.

Table S1 Comparison of the comprehensive performance of this work with other reported advanced Marangoni actuators.

Actuation module	Velocity (mm s^{-1})	Propulsion Method	Shape	Size	Mass	Actuation duration	Controllability
Vanillin[1]	15	Chemical-driven	Rectangle	1 cm × 2 cm	/	50 min	Low
Glucose[2]	16	Chemical-driven	Round-bottom flask-shaped	10 µm	/	90 min	Low
Camphor[3]	19	Chemical-driven	Boat	8 cm	1.375 g	≥25 min	Low
MXene/LDPE[4]	2.9	Light-driven	/	/	/	1 min	High
Sunflower pollen grain[5]	0.3	Light-driven	Sphere	40 µm	47 mg	/	High
Au-pNIPAM[6]	0.7	Light-driven	Rectangle	4 mm × 15 mm	/	/	High
Liquid metal droplets[7]	126	Electrical-driven (21 V)	Sphere	3 mm	/	≥20 min	High
Foam-core liquid metal[8]	34	Electrical-driven (9 V)	Hemisphere	5 mm	2.5 mg	≥20 h	High
SACNT[9]	20	Electrical-driven (4 V)	Bullet-shaped	5 cm	3.06 g	6 min	High
	16	Light-driven				/	High
Graphene oxide foam[10]	8	Light-driven + Magnetic field	Pentagram	2 cm	15.9 mg	/	High
CNT-CF	**5.4**	**Electrical-driven (3.7 V)**	**Bullet-shaped**	**5 cm**	**3.8 g**	**20 min**	**High**
	11.3	**Chemical-driven**				**3-4 min**	**Low**
	32.2	**Electrical + Chemical dual-driven**				**90 s**	**High**

References

[1] Zhou, J.; Zhang, Y.; Zhang, M.; Yang, D.; Huang, W.; Zheng, A.; Cao, L. High-performance MXene hydrogel for self-propelled Marangoni swimmers and water-enabled electricity generator. *Adv. Sci.* **2025**, *12*, 2408161.

[2] Yan, M.; Arsyad, R.; Putri Namari, N. A.; Suzuki, H.; Takeyasu, K. Mixed-potential-driven catalysis in glucose oxidation. *ChemCatChem* **2024**, *16*, e202400322.

[3] Lin, C.; Kinane, C.; Zhang, Z.; Pena-Francesch, A. Functional chemical motor coatings for modular powering of self-propelled particles. *ACS Appl. Mater. Interfaces* **2022**, *14*, 39332-39342.

[4] Luo, X.; Li, L.; Zhang, H.; Zhao, S.; Zhang, Y.; Chen, W.; Yu, Z. Multifunctional $Ti_3C_2T_x$ MXene/low-density polyethylene soft robots with programmable configuration for amphibious motions. *ACS Appl. Mater. Interfaces* **2021**, *13*, 45833-45842.

[5] Song, L.; Cai, J.; Zhang, S.; Liu, B.; Zhao, Y.; Chen, W. Light-controlled spiky micromotors for efficient capture and transport of targets. *Sens. Actuator B-Chem.* **2022**, *358*, 131523.

[6] Sepúlveda, A.; Boudreau, D. Neighbors Matter: Leveraging collective thermoplasmonic effects for smart soft actuators. *ACS Appl. Polym. Mater.* **2024**, *6*, 2359-2370.

[7] Fuchs, R.; Abdoli, S.; Kilani, M.; Nor-Azman, N.; Yu, R.; Tang, S.; Dickey, M. D.; Mao, G.; Kalantar-Zadeh, K.; Tang, J. Stroking through electrolyte: liquid metal droplet propulsion through pulse time modulation. *Adv. Funct. Mater.* **2024**, *34*, 2314815.

[8] Chen, Y.; Chen, X.; Zhu, Z.; Sun, M.; Li, S.; Gan, M.; Tang, S.; Li, W.; Zhang, S.; Sun, L.; Li, X. 3D actuation of foam-core liquid metal droplets. *Soft Matter* **2023**, *19*, 1293-1299.

[9] Lin, H.; Qian, Y.; Zhou, P.; Lin, J.; Luo, Z.; Zhang, W.; Chen, L. Electricity-driven strategies for bioinspired multifunctional swimming Marangoni robots based on super-aligned carbon nanotube composites. *Small* **2024**, *20*, 2400906.

[10] Wang, W.; Shao, W.; Li, N.; Guo, H.; Zeng, S.; Zhang, Y.; Zhang, J.; Han, D.; Zhang, Y. Graphene oxide foam-based floating actuators manipulated via dual-Marangoni-effect propulsion and magnetic-field-guided navigation. *Small Methods* **2025**, *9*, 2401946.

Movie S1. Linear motion of the electrical-driven Marangoni actuator.

Movie S2. Turning-left motion of the electrical-driven Marangoni actuator.

Movie S3. Turning-right motion of the electrical-driven Marangoni actuator.

Movie S4. Motion of the chemical-driven Marangoni actuator.

Movie S5. Motion of the dual-driven Marangoni actuator.

Movie S6. A crawling actuator.

Movie S7. A robotic gripper.